University of Baghdad
College of Engineering

Journal of Engineering

journal homepage: www.jcoeng.edu.iq

Volume 32 Number 9 September 2026

Synergistic and Antagonistic Effects of Nanoparticle Deposition in Low-Concentration Mono and Hybrid Nanofluids for Pool Boiling Heat Transfer

Rahma Sh. Kadhim *, **Ekhlas M Fayyadh**, **Qahtan A. Al-Nakeeb**

College of Mechanical Engineering, University of Technology, Baghdad, Iraq

ABSTRACT

The ever-increasing heat dissipation requirements of modern high-performance electronics critically demand advanced cooling techniques beyond conventional fluids. Nanofluids have emerged as a next-generation solution for enhanced boiling heat transfer. This study experimentally investigates the pool boiling performance of mono- and hybrid nanofluids at a low volume concentration of 0.01% on a smooth copper surface under saturated conditions using deionized water (DIW) as the base fluid. Three mono nanofluids (Al_2O_3/DIW, Ag/DIW, and GNPs/DIW) and three compositions of hybrid nanofluids with a constant mixing ratio of 50:50 (Al_2O_3-Ag/DIW, Al_2O_3-GNPs/DIW, and Ag-GNPs/DIW) were prepared. The critical heat flux (CHF) and heat transfer coefficient (HTC) were systematically analyzed. All nanofluids enhanced boiling performance compared with deionized water. Among the mono nanofluids, GNPs/DIW achieved the highest enhancement, increasing CHF and HTC by 40.55% and 164.8%, respectively. The hybrid nanofluid Ag-GNPs/DIW exhibited the better overall performance, enhancing CHF and HTC by 53.63% and 209.8%, respectively. Conversely, the Al_2O_3-GNPs/DIW hybrid nanofluid exhibited decreasing heat transfer performance compared with Mono-GNPs/DIW, indicating opposite deposition effects caused by the Al_2O_3 added. Characterization of the surface using SEM, EDS, XRD, contact angle, and porosity detects that GNP deposition creates a protective graphitic layer that minimizes copper oxidation and enhances surface porosity and cavity radius, consequently enhancing boiling heat transfer. In contrast, Al_2O_3 encourages oxide formation and partial pore blockage, which reduced HTC. These results provide new insights into synergistic and antagonistic nanoparticle deposition mechanisms that control the enhancement of boiling in mono- and hybrid nanofluids.

Keywords: Critical heat flux, Deposition, Hybrid, Heat transfer coefficient, Nanofluids.

1. INTRODUCTION

The rapid development of high-performance industrial equipment and thermal systems that improve HT efficiency has been essential in numerous engineering applications, such as

*Corresponding author
Peer review under the responsibility of University of Baghdad.
https://doi.org/10.31026/j.eng.2026.09.08

Article received: 07/07/2026
Article revised: 28/08/2026
Article accepted: 29/08/2026
Article published: 01/09/2026

cooling systems, power generation, high-density electronics, and advanced thermal systems. Two-phase systems are particularly effective, enabling heat removal rates of up to (100 kW/m^2). However, the HF generated by the latest generation of microelectronic devices has exceeded 15,000 kW/m^2 **(Saha, 2016; Xiao et al., 2023)**, creating a significant challenge for conventional cooling techniques. Moreover, traditional fluids, like ethylene glycol, water, thermal oils, and water, possess very low Thermal Conductivity (TC) and the inability to respond to high heat fluxes (q''); thus, restrictions on supporting the current cooling requirements. To overcome these gaps, NFs have come up as an attractive method to augment the thermophysical properties of Base fluids (BFs) and to minimize the total thermal resistance. Numerous studies **(Vajjha and Das, 2009; Li et al., 2020; Maheshwary et al., 2020; Ali, 2022; Karikalan et al., 2022; Mostafizur et al., 2022)** confirm that nanoparticle addition improves both TC and other physical properties influencing heat transfer performance. Despite these advantages, boiling HT performance, particularly the HTC and CHF are strongly influenced via many parameters, like wettability, concentration of particles, and size. Among these, nanoparticle deposition on the heated surface plays a crucial role. And, in higher concentrations, the deposition may form thick layers or smooth out the surface, reducing surface roughness and suppressing nucleation sites, thereby deteriorating HTC. On the other hand, moderate deposition may benefit CHF by altering surface topography, raising porosity, and raising wettability. For instance, **(You et al., 2003)** reported CHF enhancement of up to 1.35 times employing SiO_2, Al_2O_3, and ZrO_2, based NFs. However, the relationship between boiling performance and the concentration of nanoparticles is highly non-linear. While **(Vafaei, 2015)** reported the HTC enhancement of up to 140% on rough surfaces, **(Manetti et al., 2017)** observed reduced performance at higher concentrations due to excessive surface smoothing. Similarly, **(Kamel and Lezsovits, 2020)** demonstrated that the low concentrations of CeO_2 and WO_3 NFs improved HTC by up to 70%, whereas higher concentrations led to performance degradation depending on surface conditions. Other studies **(Golkar et al., 2021**; **Wen et al., 2023**; **Du et al., 2024)** confirmed that although HTC may decrease at high concentrations, CHF can still improve significantly due to enhanced wettability and delayed vapor blanket formation. Furthermore, wettability is another governing parameter in boiling HT. **(Kwark et al., 2010)** noted that the HTC decreases with increasing the concentration of nanoparticle, even under very low volume fractions. **(Quan et al., 2017)** showed that moderately hydrophilic nanoparticles improve HT by increasing bubble departure frequency, whereas highly hydrophilic particles can degrade performance. **(Mukherjee et al., 2021)** summarized this "wettability contradiction," highlighting the trade-off between improved wettability and excessive deposition, which reduces the nucleation site density.

MNFs, consisting of a single type of nanoparticle, are inherently limited because no single material can simultaneously provide high TC (metals), porous structures (oxides), and nanoscale surface texturing (carbon-based materials). To address these limitations, HNFs have been developed via the dispersion of two or more types of nanoparticles into a BF. This approach enables synergistic enhancement of thermophysical properties, wettability, stability, and surface tension, thermal conductivity **(Moldoveanu et al., 2018; Mousavi et al., 2019; Kumar et al., 2020; Vicki et al., 2020; Gao et al., 2021; Akhtar et al., 2022; Borode et al., 2023; Selvarajoo and Wanatasanappan, 2024; Nazir et al., 2024; Shaik et al., 2024)**. Experimental studies on the HNFs have demonstrated promising results. **(Reddy and Venkatachalapathy, 2018)** reported CHF enhancement of 49.84% using Al_2O_3-CuO/DIW NFs at 0.1 vol%, although HTC improvement was limited at lower concentrations.

Similarly, **(Sharma et al., 2021; Gupta and Misra, 2023)** depicted an important improvement in the HTC and CHF for Cu-ZnO and Ag-ZnO HNFs, particularly at higher concentrations. Surface modification further amplifies these effects, as demonstrated by **(Sharma and Unune, 2023)**, who reported fundamental enhancements in CHF and HTC on roughened surfaces. The HNFs' performance is strongly influenced by the combination of nanoparticle types. Oxide-oxide and carbon–oxide hybrid combinations generally perform well at low concentrations, while metal–oxide combinations often need higher concentrations for substantial enhancement. Recent studies have highlighted the potential of HNFs for enhancing the PB HT through synergistic effects between different nanoparticle types. For instance, **(Mehralizadeh et al., 2020)** documented that TiO_2-SiO_2 HNFs effectively balance thermal conductivity and wettability, causing an important improvement of the HTC. Similarly, **(Sezer et al., 2020)** demonstrated that GNP-Ag HNFs improved the CHF and HTC via 123.5%, and 109%, respectively, due to the increased density of nucleation sites and the enhanced surface hydrophilicity. **(Kamel et al., 2021)** also observed improved the PB HT performance with Al_2O_3-CeO_2 NFs, attributing the enhancement to the conductive nano-porous layer creation upon the heating surface. In addition, **(Ma et al., 2022)** revealed that incorporating hydrophilic nanoparticles, such as Al_2O_3 and SiO_2 into GNP-Fe_3O_4 HNFs promotes porous structure formation, increasing bubble generation and HTC, while improved wettability contributes to CHF enhancement. More recently, **(Ajeeb and Murshed, 2023)** reported that the BN-SiO_2 HNFs enhanced HTC by up to 52% and CHF by 69%, primarily due to the nanoparticle deposition that increases the nucleation site density. A summary of previously published results on HNF PB is presented in **Table 1.**

Despite extensive research on pool boiling heat transfer enhancement using nanofluids, most prior studies have examined either mono-nanofluids or a limited set of hybrid combinations, each tested under different operating conditions, mixing ratios, and nanoparticle concentrations, making direct comparisons across studies unreliable. This limitation is particularly evident for Ag-GNP systems: **(Sezer et al., 2020)** reported substantial CHF and HTC enhancement using GNP-Ag hybrid nanofluids, but at a fixed 10:1 GNP: Ag ratio and an ultra-low concentration (0.00005–0.005 wt%), and evaluated this system independently of other particle-type pairings or their corresponding mono-nanofluids. Consequently, it remains unclear whether such enhancement arises primarily from the metal-carbon synergy itself or from the specific ratio and concentration employed. To address this gap, the present study provides a controlled experimental comparison of three mono-nanofluids (Al_2O_3/DIW, Ag/DIW, GNPs/DIW) and three hybrid nanofluid classes, namely oxide-metal (Al_2O_3-Ag), oxide-carbon (Al_2O_3-GNPs), and metal-carbon (Ag-GNPs), at a fixed low concentration (0.01 vol%) and constant mixing ratio (50:50), under identical operating and surface conditions. This design isolates the effect of nanoparticle type from confounding compositional and concentration effects, enabling a clearer attribution of heat transfer enhancement to the specific roles of Ag (thermal conductivity), Al_2O_3 (stability and porosity), and GNPs (surface structuring). Finally, nanoparticle deposition and surface evolution on an initially smooth copper surface were systematically examined to clarify the interactions among surface wettability, roughness evolution, nucleation-site activity, and boiling heat-transfer enhancement (CHF and HTC).

Table1. Literature review of experimental investigations employing HNFs.

Author	Based fluid/ Surfactant	Nanoparticle /Size (nm)	Concentration (Φ) %/Mixing Ratio	Heating element	Result
(Reddy and Venkatachalapathy, 2018)	DIW	CuO – Al_2O_3/ 50	0.01, 0.03, 0.05, 0.08, and 0.1vol%/ 50:50	Cu square	(CHF and HTC)↑ at Φ 0.1 compared to water HTC ↑ 7.1% at 0.01
(Mehralizadeh et al., 2020)	DW and a DW-EG (60:40)	TiO_2 - SiO_2/ 25–30 nm, 12 nm	0.05vol%/ (25:75, 50:50, and 75:25)	Cu cylindrical	HTC ↑ at Φ 0.05%, HTC for DW is higher at 50:50
(Sezer et al., 2020)	DIW	GNPs-Ag/-	0.00005,0.0005, & 0.005wt%/ 10:1	Cu square	(HTC, CHF) ↑ at 0.00005 wt%
(Kamel et al., 2021)	DIW	Al_2O_3 - CeO_2/20,50	0.01 to 0.1vol% / 50:50	Cu cylindrical	HTC ↑ 37% at Φ 0.05%
(Sharma et al., 2021)	DIW	Ag-ZnO/20	0.02, 0.06, and 0.1vol%/ 50:50	Cu cylindrical	(HTC, CHF) ↑ 179.92 and 65.51%, respectively, at Φ 0.1
(Ma et al., 2022)	DIW	GNP-Fe_3O_4, (Al_2O_3, SiO_2)/ (500 -5000), (100-200)	0.0005, 0.001, 0.002, & 0.003wt%/ 1:1	Cu cylindrical	(HTC, CHF) ↑ at 0.003wt% compared to DIW
(Ajeeb and Murshed, 2023)	DW-EG (85:15)	BN- SiO_2/ 70nm -20nm	0.05vol%/01:0.04, 0.02: 0.03, 0.03:0.02, and 0.04:0.01	Ni-Cr wire	(HTC and CHF) ↑ at increasing BN concentration
(Gupta and Misra, 2023)	DIW	Cu-ZnO/-	0.025,0.050, 0.075, and 0.1vol%/50:50	Cu cylindrical	(HTC and CHF) ↑ at Φ 0.1 vol%
(Sharma and Unune, 2023)	DIW	Ag-ZnO/-	0.02, 0.06, and 0.1vol%/ 50:50	Cu cylindrical	(CHF, HTC) ↑ at Φ 0.1%.

2. MATERIALS AND METHODS

2.1 Pool Boiling System of The Experiment

The pool boiling experimental apparatus is illustrated photographically and schematically in **Fig. 1(A and B)**. The pool boiling facility comprises a boiling chamber, heating system, cooling unit, power supply unit, and data acquisition. A boiling chamber was made from stainless steel with a 132 mm outer diameter, 6 mm thickness, and 230 mm height. Two viewing windows are available at the front and rear of the side wall chamber for visualization. The chamber was fixed between the grooves engraved in the top stainless steel and bottom Teflon flanges with an O-ring and steel rods to support and prevent leakage of working fluid. The top flange features various functional ports, including a water inlet, a vacuum port, a pressure gauge, a type K thermocouple probe to measure the bulk temperature, and a water-cooling condenser. The cooling coil has a helical stainless-steel tube of 6 mm diameter to condense and return the vapor generated. The heating system consists of an auxiliary heater and a main heat flux generator. For heating the working fluid and maintaining a saturation temperature of the fluid, two auxiliary cartridge heaters, each (200 W), were installed at the bottom Teflon flange. And controlled by a temperature controller (PID) with a K- type thermocouple. The heat flux (HF) generator comprises a copper (Cu) heating block, a Cu test surface, and eight cartridge heaters each (250 W). The Cu heating test surface is 20 mm in diameter and 70 mm high. It contains five K-type thermocouples (RS-Pro Company) calibrated to an accuracy of (± 0.1 °C) for estimating the temperature of the wall and HF. And the thermocouple plugs into (1 mm) diameter holes (filled with a thermal component having a thermal conductivity of (8.5 W/m.K) to avoid the air gaps) at the Cu test surface radial central, as shown in **Fig. 2**. A copper test surface was secured upon the Cu heating assembly (Cu heating block with eight inserted cartridge heaters) with a screwing arrangement. Thermal paste was applied to the threaded section of the test surface to ensure good thermal contact with the heating assembly. This combined assembly was tightly fitted into the space offered by the bottom flange. The remaining part of the copper test surface and the heating assembly were insulated with Teflon and thermal wool, respectively, to reduce heat loss to the surroundings. Similarly, the entire chamber, except for the viewing windows, was insulated by elastomeric foam. A Data Logger (Model AT4524, Apple Instruments Company) was used to record temperature data in real time; it was connected to the laptop via software installed on the laptop to collect all data. However, power was supplied to two variable transformers (Variac) (Model HSN 0103 220 PLUG). One of them was linked to the PID controller to regulate the power supplied to an auxiliary heater. The others, which were connected to a stabilizer, were supplied to the cartridge heater.

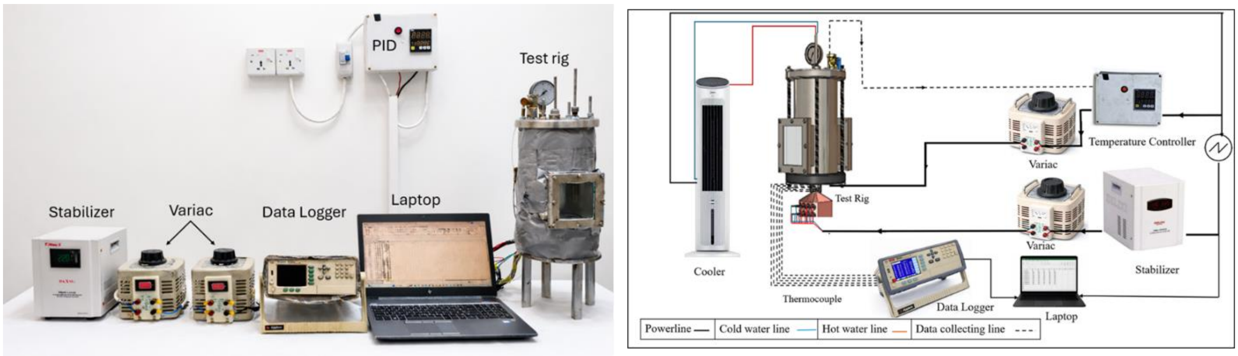

(A) (B)

Figure 1. (A) The experimental facility and (B) Schematic diagram of the experimental testing loop.

1. Pressure gauge
2. Ventilation valve
3. Upper flange
4. Condenser coil
5. Stainless steel chamber
6. Rod
7. Glass window
8. Lower flange
9. Auxiliary heater
10. Copper heating test surface
11. Copper heating Block
12.Cartridge heaters
13. Bouch Teflon

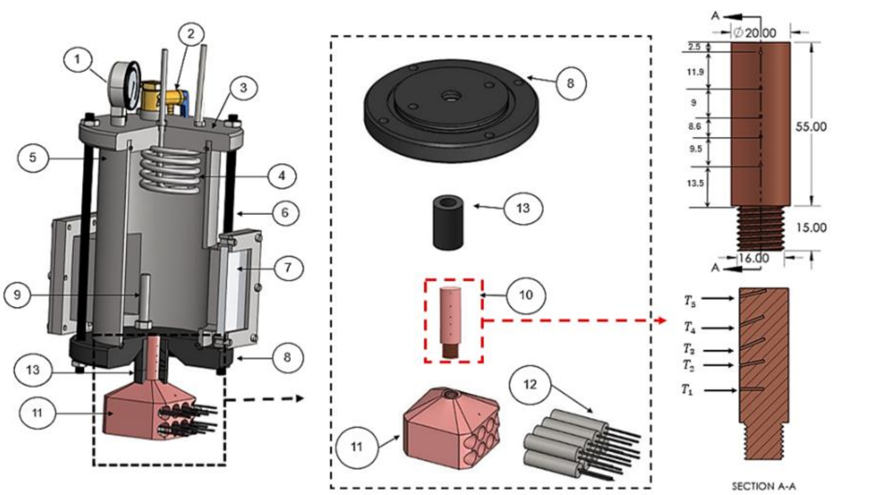

Figure 2. Experimental setup and test section.

Table 2. Properties of nanomaterials

Material	Particle size, nm	Shape	Purity	Color	Thermal conductivity W/m. K	Density, g/ml	Specific surface area, m^2/g
Al_2O_3	~50	Spherical	99.9%	White	30	3.98	25-35
Ag	20-50	Spherical	> 99%	Grey	420	10.49	5-20
GNPs	Thickness per layer (0.34)	Sheet	>99%	Black	3100	2.27	100-700

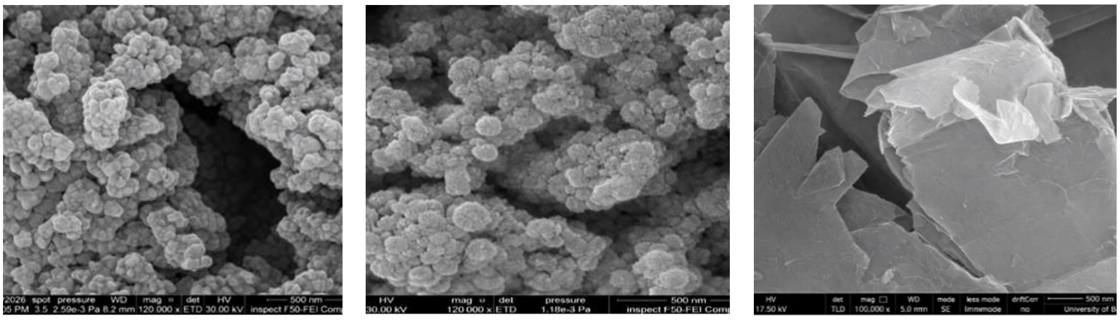

Al_2O_3 Ag GNPs

Figure 3. Scanning Electron Microscope (SEM) image of nanoparticles.

2.2 Nanoparticle Materials and Characteristics

Three types of nanoparticles are used: silver (Ag), aluminum oxide (Al_2O_3), and graphene (GNPs), which were obtained from Sky Spring Nanomaterials, Inc. The material properties were summarized in **Table 2**. To characterize the morphological properties of the nanoparticles, Scanning Electron Microscopy (SEM) and X-ray Diffraction (XRD) were used. The SEM in **Fig. 3** shows that the Al_2O_3 nanoparticles appeared spherical, with a diameter of 53 nm. Similarly, the Ag nanoparticles appeared spherical, with a mean diameter of about 25 nm. Additionally, the GNPs were plate-shaped, with dimensions of about 950 nm and a thickness of 0.34 nm. Furthermore, the sharp diffraction peaks observed in **Fig. 4** indicate high crystallinity of the nanomaterial and the absence of crystalline impurities and secondary phases.

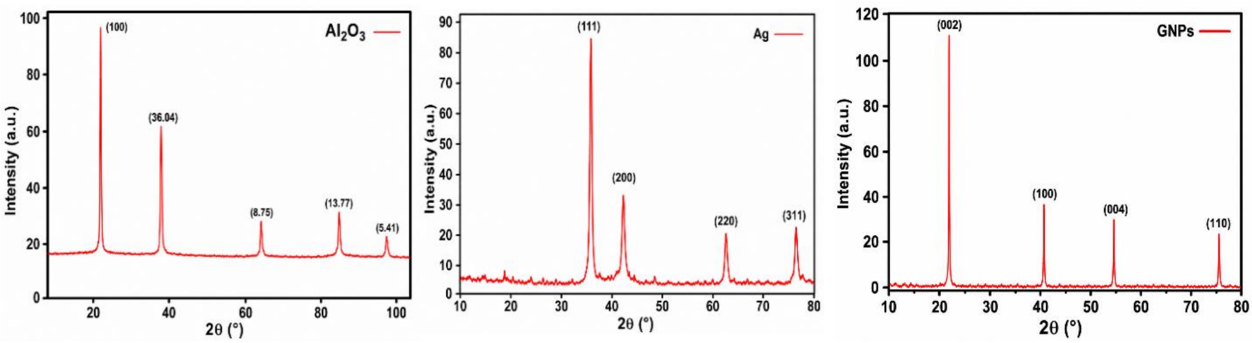

A B C

Figure 4. X-ray diffraction patterns of the (A) Al_2O_3, (B) Ag, and (C) GNPs nanoparticles. The diffraction patterns confirm the crystalline structure and phase purity of the nanoparticles.

2.3 Nanofluid (NF) Preparation and Characteristics

In the present work, three mono-nanofluids (Al_2O_3/DIW, Ag/DIW, and GNPs/DIW) and three hybrid nanofluids (Al_2O_3-Ag, Al_2O_3-GNPs, and Ag-GNPs) were prepared at a fixed volume fraction of 0.01%. For the hybrid nanofluids, the total nanoparticle concentration was fixed at 0.01 vol.%, while the mixing ratio of the two constituent nanoparticles was fixed at 50:50 (by volume), resulting in a concentration of 0.005 vol.% for each nanoparticle. This equal ratio was selected to ensure an equal contribution from each component, preventing either component from dominating the hybrid's physicochemical response (thermal conductivity, wettability, and surface structuring). This constant, equal-weight ratio across all three hybrid classes allows the observed differences in HTC and CHF to be attributed to nanoparticle-type interactions rather than to compositional weighting. A two-step method was used to prepare the working fluids (mono- and hybrid nanofluids) required for testing. For each mono-nanofluid, the preparation procedure, shown in **Fig. 5**, is as follows: (i) Dispersion of the desired amount of surfactant in DIW, Arabic Gum (AG), and Sodium Dodecyl Sulfate (SDS) was used as stabilizing agents at a 1:1 mass ratio (AG: SDS = 1:1, w/w) at a total nanofluid concentration of 0.01 vol%. This ratio was selected based on established nanofluid preparation practice, where AG provides steric stabilization **(Mohamed et al., 2025)**, and SDS provides electrostatic repulsion to prevent nanoparticle agglomeration **(Jalilov et al., 2026)**. They are employed to improve nanoparticle dispersion stability **(Abid and Getan, 2010)**. And, the dispersal is magnetically stirred (MS300HS) for (15 min) at (700 rpm) for obtaining a totally dissolved and homogenous mix of surfactant in the base fluid, **(Ebrahim, 2023)**; (ii) Using an analytical balance (Kern ABT 120-4NM) to weigh the nanoparticle (NP) according to equation (1); (iii) Adding the weighted NP to the resultant mix, pursued via the magnetic stirring procedure, which is conducted for 1 to 2 h at 260-750 rpm depending on the type of NP, **(Parui, 2020)**; (iv) The latter mixture is taken to an ultrasonic bath (Skymen Ultrasonic JP-009 1.3 L) for 1 to 3 h at 450 kHz and a temperature of 40°C. For HNF preparation, the corresponding mono nanofluids were mixed in equal volumes and subsequently ultrasonicated for 1–2 h, operating intermittently (10 seconds on/10 seconds off) to minimize heat accumulation and excessive temperature rise during sonication, to ensure proper mixing and obtain a visually homogeneous dispersion, yielding hybrid nanofluids at a total concentration of 0.01 vol.%. The sonication duration was adjusted according to the nanoparticle combination and the time required to achieve homogeneous dispersion. Hybrid nanofluids containing GNPs required a relatively longer sonication time due to strong van der Waals interactions and their tendency to restack, whereas Al_2O_3-containing nanofluids were more readily dispersed.

$$\phi = \frac{\left(\frac{m_{np}}{\rho_{np}}\right)}{\left(\frac{m_{np}}{\rho_{np}}\right)+\left(\frac{m_{BF}}{\rho_{BF}}\right)} \times 100 \quad (1)$$

Transmission Electron Microscopy (TEM) images of the nanofluids were obtained to examine nanoparticle shape and size, as shown in **Fig. 6**. These images confirm that the nanoparticles were well dispersed within the base fluid, and the observed particle sizes were consistent with the specified values.

2.4 Stability of Nanofluid

The stability of NF (MNFs and HNFs), the nanoparticle deposition in the BF over time was visually investigated, as shown in **Fig. 7**. According to the figure, MNFs and HNFs had good stability after 35 days. Furthermore, the outcome of zeta potential, measured using a Brookhaven Zeta Plus (Brookhaven Instruments, USA), illustrated in **Fig. 8** shows that the samples of NFs preparation have good stability, with zeta potentials of Al_2O_3/DIW (-31± 0.03 mV), Ag/DIW (-45± 0.03mV), and GNPs/DIW (45± 0.03 mV). Moreover, HNF Al_2O_3-Ag/DIW has very good stability (50± 0.03 mV), Al_2O_3-GNPs/DIW (46± 0.03 mV), and Ag-GNPs/DIW (53 ± 0.03 mV). The result confirms the finding of **(AlMuhaysh et al., 2025),** who reported that potential values greater than ±30 mV are estimated to be very stable, while the values above 45 mV indicate superior stability. It is noteworthy that the boiling experiments were carried out one day after the NFs preparation.

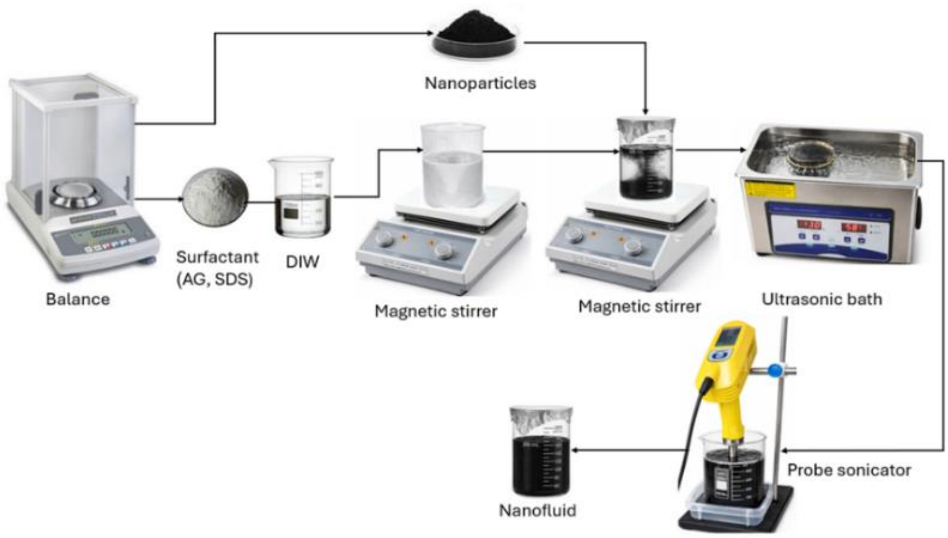

Figure 5. Schematic of nanofluid preparation procedure.

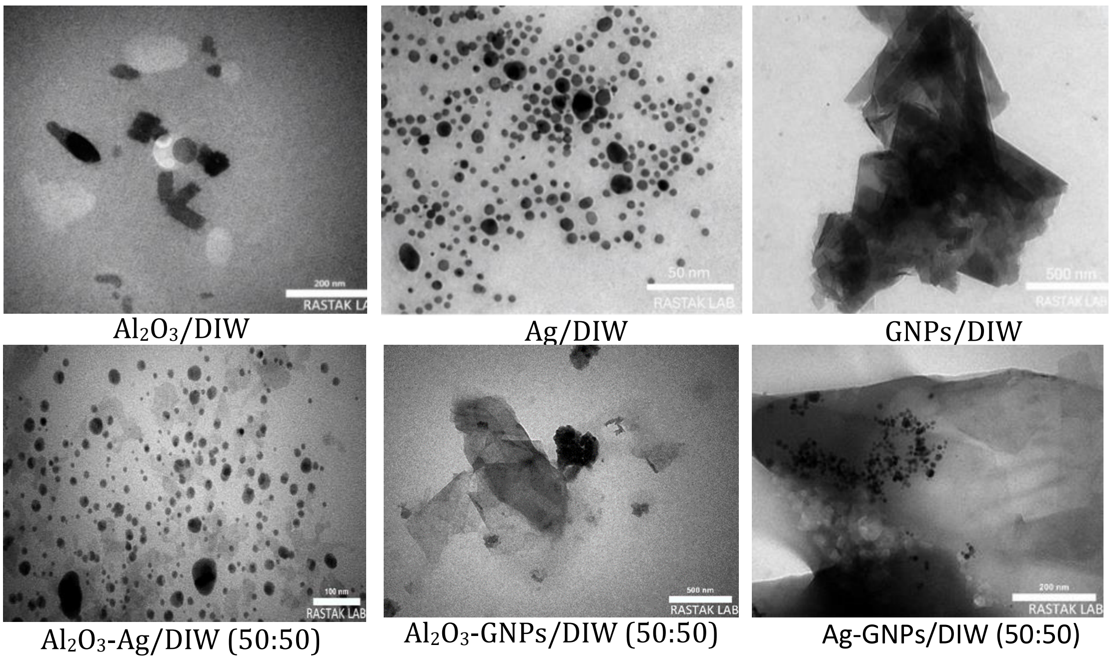

Figure 6. Transmission electron microscopy (TEM) images for Mono and Hybrid nanofluids.

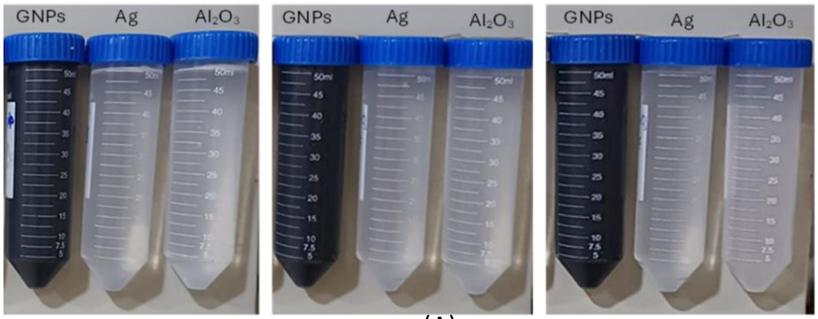

(A)

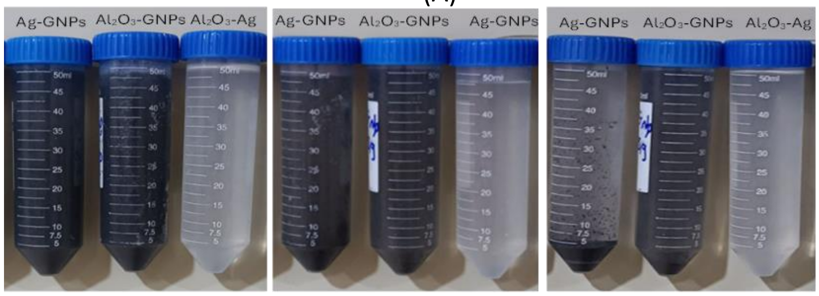

1Day 15Days 35 Days

(B)

Figure 7. Visual stabilization of nanofluids for: (A) Mono nanofluids and (B) Hybrid nanofluids. Illustrates the sedimentation behavior over the observation period (1 day, 15 days, and 35 days).

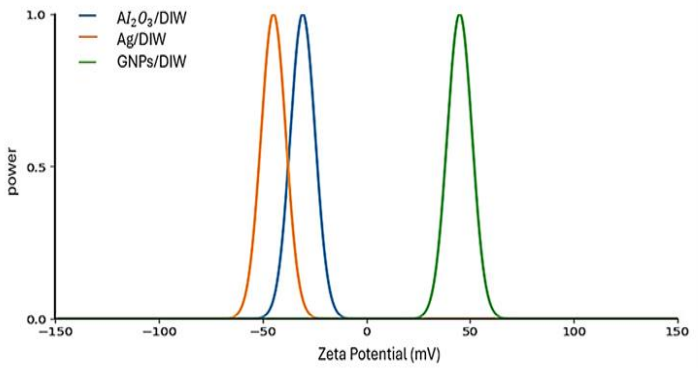

(A)

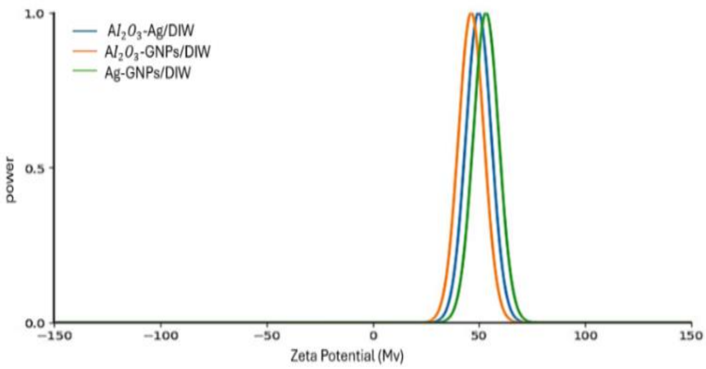

(B)

Figure 8. Measurement of Zeta Potential for: (A) Mono nanofluids and (B) Hybrid nanofluids. This indicates the electrostatic stability of the nanofluids.

2.5 The Experimental Procedure

The experiments were conducted using various working fluids (WF), namely, deionized water, mono nanofluids, and hybrid nanofluids, under saturated conditions. Seven of copper test surfaces were prepared, with one dedicated surface for each working fluid: one for DIW, three for MNFs, and three for HNFs. Thus, each working fluid was tested on a separate, initially smooth copper surface to avoid cross-contamination and ensure comparable initial surface conditions. For the three repeated experiments conducted with the same working fluid, the corresponding dedicated copper test surface was reused after thorough cleaning to remove any nanoparticle deposition and restore comparable initial surface conditions. Before each test, the boiling chamber and test section were thoroughly cleaned with soap and DIW to remove any residual deposits and dirt from the chamber and other components, and were then filled with WF. Following this, to heat the working fluid to the saturation temperature, the auxiliary heaters were switched on and controlled with an autotransformer supplied by an AC source; the ventilation valve on the top flange was opened to release any dissolved gases. The saturation temperature was maintained for 30–45 min to remove any dissolved gases from the working fluid. A condensing coil was located on the upper flange to condense any vapor back into the chamber to ensure no loss of working fluid during experimentation. Once the test stabilized, the valve was closed, then the input power to the cartridge heaters was switched on and supplied gradually by a variac of capacity 9 A and 220 V. Measurements of electrical power were taken by an ammeter and a voltmeter. The next increment of input power was applied after the stable condition was characterized by a temperature variation within the measurement uncertainty (±0.1°C) for over 1 min, as mentioned by **(Al-obaidy et al., 2024)**. Tests were conducted by incrementally increasing the applied voltage in steps of 5 V, with each voltage level maintained for approximately 15–20 minutes until steady state was reached to the next increment. Once a steady state was achieved, temperature readings were acquired from the thermocouples via a data acquisition system at 10 s intervals. The critical heat flux (CHF) condition was identified by a sudden and pronounced increase in the copper test wall temperature relative to the preceding readings. At this point, the heater power was immediately switched off, and the corresponding temperature data were recorded. Each operating condition was repeated three times, and the average value was calculated to ensure repeatability.

3. DATA REDUCTION AND UNCERTAINTY

In the boiling system, the heat flux transfer is assumed in the axial direction. The temperature of the heated surface can be calculated by a one-dimensional heat conduction equation(i.e., Fourier's law **(Holman, 2010)**, as indicated in Eq. (2):

$$q'' = -k * \left(\frac{dT}{dy}\right) \tag{2}$$

Where, q'' is the heat flux, and k is the thermal conductivity of the copper heating block, which is equal to (395 W/m K). And $\frac{dT}{dy}$ is a temperature gradient that is determined from the four-point backward Taylor's series approximation, **(Anderson et al., 1984)**, as given in Eq. (3):

$$\frac{dT}{dy} = \frac{(11*T_4)-(18*T_3)+(9*T_2)-(2*T_1)}{6*dy} \tag{3}$$

Where T_4, T_3, T_2, and T_1 are the temperatures measured in the vertical direction on the copper test surface, as shown in **Fig. 2**. The distance between the thermocouple, dy is 11mm.The boiling surface temperature (T_s)The copper heated test was determined using Eq. (4):

$$T_s = T_5 - \left(\frac{q''y}{k}\right) \quad (4)$$

Where T_5 is the measured temperature of the thermocouple that is underneath the heating test surface, and y is the distance between T_5 and the boiling surface; y is equal to 1mm.

The heat transfer coefficient (h) is calculated as follows:

$$h = \frac{q''}{(T_s - T_{sat})} \quad (5)$$

Where T_{sat} is the saturation temperature of the deionized water.

The HF estimated from the electrical supply was calculated as follows:

$$q'' = \frac{(V * I)}{A} \quad (6)$$

Where V, I, and A are the applied voltage and electric current of the experimental heater, and the surface area of the heating test surface, respectively. However, the heat flux estimated from Eq.6 and that calculated by Eq.2 were compared to indicate the amount of heat losses along the heater block.

Uncertainty of the heat flux (Uq) and heat transfer coefficient (Uh) can be determined based on the uncertainty propagation law, **(Coleman and Steck, 1989),** as given below:

$$Uq = \left[\left(\frac{\partial q}{\partial T_1} \cdot UT_1\right)^2 + \left(\frac{\partial q}{\partial T_2} \cdot UT_2\right)^2 + \left(\frac{\partial q}{\partial T_3} \cdot UT_3\right)^2 + \left(\frac{\partial q}{\partial T_4} \cdot UT_4\right)^2\right]^{\frac{1}{2}} \quad (7)$$

$$Uh = \left[\left(\frac{\partial h}{\partial q} \cdot Uq\right)^2 + \left(\frac{\partial h}{\partial Ts} \cdot UT_s\right)^2 + \left(\frac{\partial h}{\partial T_{Sat}} \cdot UT_{Sat}\right)^2\right]^{\frac{1}{2}} \quad (8)$$

$$U_{(T_s)} = \left[\left(\frac{\partial T_s}{\partial T_5} \cdot U_{(T_5)}\right)^2 + \left(\frac{\partial T_s}{\partial q''} \cdot U_{(q'')}\right)^2 + \left(\frac{\partial T_s}{\partial y} \cdot U_y\right)^2 + \left(\frac{\partial T_s}{\partial k} \cdot U_k\right)^2\right]^{(1/2)} \quad (9)$$

The resulting uncertainty was approximately the heat transfer coefficient, heat flux, and boiling-surface temperature, ± 5.8%, ± 5.2%, and ±0.13. The uncertainty values are summarized in **Table 3**.

Table 3. The experimental uncertainties

Quantity	**Uncertainty**
AC Voltage	± 1 V
AC Current	± 0.2 A
Temperature	± 0.1^{o}C
Ts	±0.13^{o}C
HTC (h)	± 5.8% (kW/m^2. K)
HF (q")	± 5.2% (kW/m^2)

4. RESULTS AND DISCUSSION

4.1 Experimental Validation

Data obtained from boiling deionized water over a flat-plate test heater have been analyzed to verify the integrity of the experimental setup. Also, these data shall be used as reference data to assess the nanofluids' pool boiling performance. The HTCs for the water pool boiling were compared with the correlations proposed by **(Cooper, 1984; Cornwell and Houston, 1994; Jung et al., 2004)**, given in **Table 4**, in addition to the previous investigational data, as illustrated in **Fig.9**. As well, the investigational data for the water boiling are determined to agree with previous work. Where the deviation of the HTC values obtained was 23.13%, 32.03%, and 38.26%, if compared with the theoretical relationship proposed via **(Cooper, 1984; Cornwell and Houston, 1994; Jung et al., 2004)**, respectively. The acknowledged prediction limitations of conventional pool boiling correlations are compatible with these physically justified deviations, which were developed under idealized smooth-surface conditions and do not account for surface roughness, heater geometry, and specific fluid-surface combination effects that characterize the current experimental configuration **(Jones et al., 2009)**. According to a thorough evaluation by **(Pioro and Rohseno, 2004),** even the most dependable correlations show significant scatter when compared to various surface and fluid combinations. Comprehensive evaluations of pool boiling prediction methods in the literature have confirmed that mean absolute errors of standard correlations can reach 25–30%, with deviations up to ±30% generally regarded as acceptable **(Li et al., 2014; Ji et al., 2015)**. Therefore, considering the surface roughness, contact angle, and heater geometry effects present in our experimental configuration, the current mean absolute errors of 23–39% relative to the Cooper, Cornwell-Houston, and Jung correlations are consistent with the documented scatter of these classical predictive tools. Furthermore, a much better agreement with previously published experimental data was obtained, with 20.35% and 18.2% when compared with the values reported via **(Sarafraz et al., 2020; Akbari et al., 2019)**, respectively. The comparison indicated that the experimental device is reliable. Observing forecasts from the relationship converges to the investigational values at increased HF due to the high bubble dynamics.

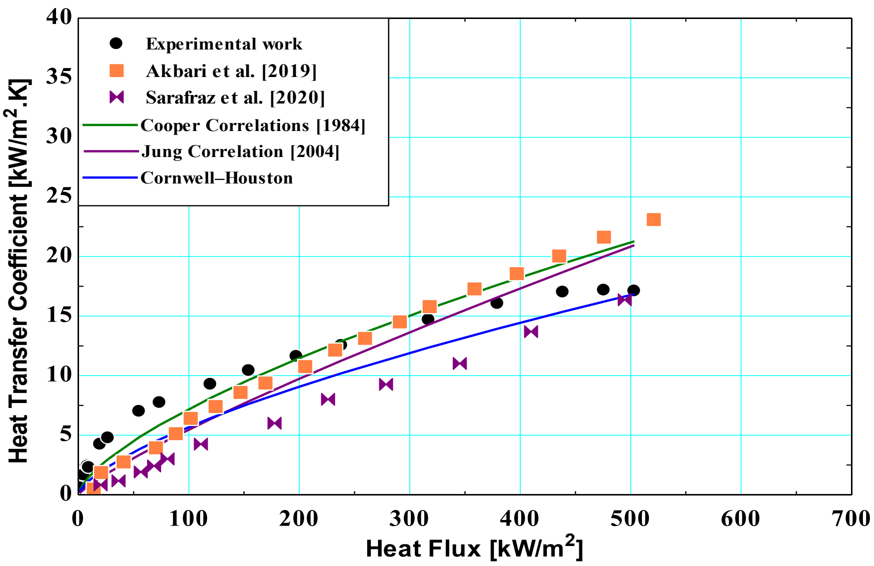

Figure 9. Comparison between the investigational data for DIW and previous work.

Table 4. The validation equations

Reference	Equations
(Cooper, 1984)	$h = 55Pr^{(0.12-0.434lnRp)}(-logPr)^{-0.55}M^{-0.5}q^{0.67}$
(Cornwel-Houston, 1994)	$Nu = 9.7P_c^{0.5}F_pRe^{0.67}Pr^{0.4}$ $Fp = 1.8P_r^{0.17} + 4P_r^{1.2} + 10P_r^{10}$ $Re_b = \frac{qD}{\mu_f h_{fg}}$ P_r is a reduced pressure $P_r = \frac{p}{pc}$
(Jung; 2004)	$h = 41.4\, k_l D_b \left(q\frac{D_b}{k_l T_{sat}}\right)^C (-log_{10}Pr)^{-1.52}\left(1 - \frac{rho_g}{rho_f}\right)^{0.53}$

4.2 Effect of Nanofluids on The Pool Boiling Characteristics

4.2.1 Effect of the Mono-type NFs

To investigate how different nanoparticle types affect boiling HT in MNFs, three MNFs were made via dispersing metal oxide (Al_2O_3) nanoparticles, metal Ag nanoparticles, and graphene nanoplatelets (GNPs), each one separately in DIW. Boiling curves and HTC curves of DIW and three types of MNFs (Al_2O_3/DIW, Ag/DIW, and GNPs/DIW) are shown in **Figs. 10 A and B**, at a (0.01 vol%) concentration. The outcomes manifested that the boiling curves and HTC of Al_2O_3/DIW, Ag/DIW, and GNPs/DIW MNFs shift considerably to the left in comparison with those of DIW. It is clear from Fig.10 that the NFs exhibited significantly lower Onset Nucleate Boiling (ONB) temperatures compared to the DIW. The recorded ONB temperatures for the NFs of GNPs/DIW, Ag/DIW, and Al_2O_3/DIW were 1.235°C, 2.529°C, and 2.848°C, respectively. This shift represents a substantial reduction in the superheat required to initiate boiling 78%, 54.84%, and 49.143% for GNPs/DIW, Ag/DIW, and Al_2O_3/DIW, respectively. Additionally, the MNFs enhance the CHF over DIW by 7.25%, 16.29%, and 40.55%, respectively. Among them, the highest CHF of (800.2 kW/m^2) is obtained for GNPs/DIW NF. However, at low superheat, where natural convection dominates, the NFs have little effect on heat flux owing to the bubble creation influence. As the heat flux increases, the influence of nanoparticle type becomes particularly apparent at the high heat flux, where a shift to the right occurs as the nanoparticles change from carbon to metal-to-metal oxide. This indicates that the Al_2O_3/DIW NF, being a metal oxide, has a lower boiling HTC. Despite this, as depicted in **Fig. 10 B**, the highest HTC values for the whole NF are higher than those for DIW, which is attributed to the enhancement in CHF. Among them, the GNPs/DIW NF achieves the highest HTC increase of 164.8%.

4.2.2 Influence of Hybrid Nanoparticles Composition

The boiling curve and the corresponding HTCs curve of HNFs of different nanoparticle compositions, metal oxide-metal (Al_2O_3-Ag), metal oxide-carbon (Al_2O_3-GNPs), and metal-carbon (Ag-GNPs) at a constant mixing ratio of 50:50 is presented in **Figs. 11 A and B**, respectively. And the boiling curve illustrates that the ONB for all compositions of HNFs shifts toward the lower wall superheat temperatures compared to the DIW of 2.017°C, 1.52°C, and 0.6591°C for Al_2O_3-Ag, Al_2O_3-GNPs, and Ag-GNPs, respectively. This reduction demonstrates that the NFs significantly lower the thermal threshold for boiling incipience over the DIW by 63.98%, 72.857%, and 88.23%, respectively. As the wall superheat temperature increases, the boiling curve of the HNFs deviates further from that of the DIW, accompanied by a significant increase in HTC. Moreover, the CHF is noticeably enhanced via 19.39%, 30.67%, and 53.63%, while the HTC is improved via 85.39%, 132.18%, and 209.78% for Al_2O_3-Ag, Al_2O_3-GNPs, and Ag-GNPs, respectively. Among the examined compositions, the metal-carbon HNF (Ag-GNPs) evinced the high enhancement in both CHF and HTC, followed by Al_2O_3-GNPs and Ag-GNPs. This outstanding performance is ascribed to the joined influence of the high TC of metal nanoparticles (Ag) and the unique structural characteristics of GNPs. These results indicate that the composition of nanoparticles take a significant role in obtaining the HNFs boiling performance

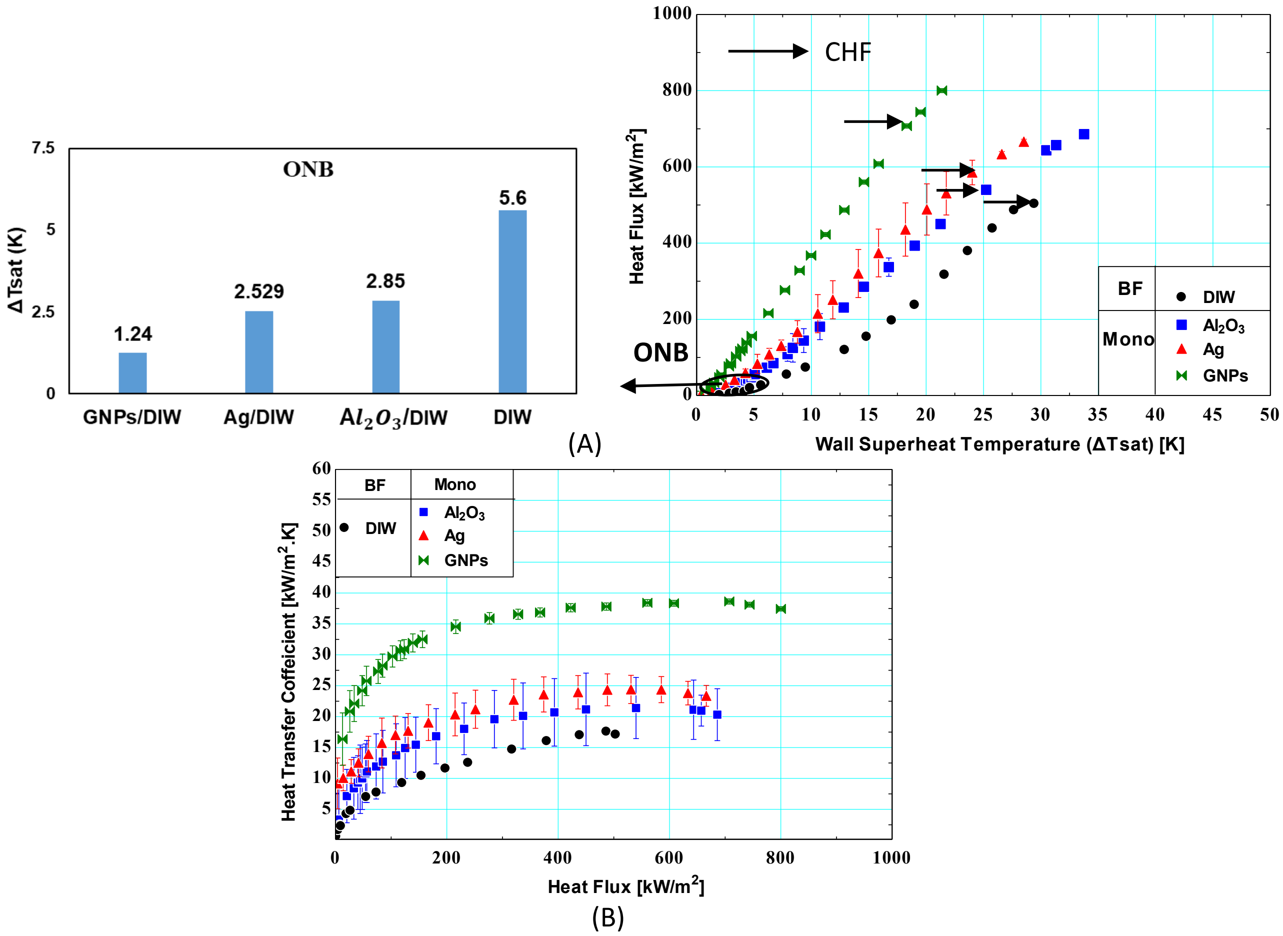

Figure 10. (A) Boiling curves and onset of nucleate boiling, and (B)Heat transfer coefficient curves of mono NFs compared with deionized.

4.2.3 Comparison of the HT Features of HNFs

Comparison of the boiling curves and corresponding HTC curves for HNFs (Al_2O_3-Ag/DIW, Al_2O_3-GNPs/DIW, and Ag-GNPs/DIW) and MNFs (Al_2O_3/DIW, Ag/DIW, and GNPs/DIW) with DIW at a constant volumetric concentration, presented in **Figs. 12 A and B**. Compared to MNFs, the HNFs (Al_2O_3-Ag/DIW and Ag-GNPs/DIW) exhibit a more pronounced improvement in HTC and CHF than their individual components. In contrast, Al_2O_3-GNPs/DIW exhibits CHF and HTC enhancement of 21.84% and 65.91%, respectively, relative to Al_2O_3/DIW; however, its performance remains slightly lower than that of GNPs/DIW alone, with reductions of 7.025% in CHF and 12.76% in HTC. In general, the Ag-GNPs/DIW

HNF showed the highest enhancement among all hybrid compositions, indicating the strong contribution of GNPs when combined with metallic nanoparticles, as manifested in **Fig. 13**. In particular, the results suggest that optimal enhancement is controlled primarily by mechanisms of surface modification induced during boiling, such as increased surface roughness, improved wettability, and higher nucleation site density, rather than only by the thermal conductivity.

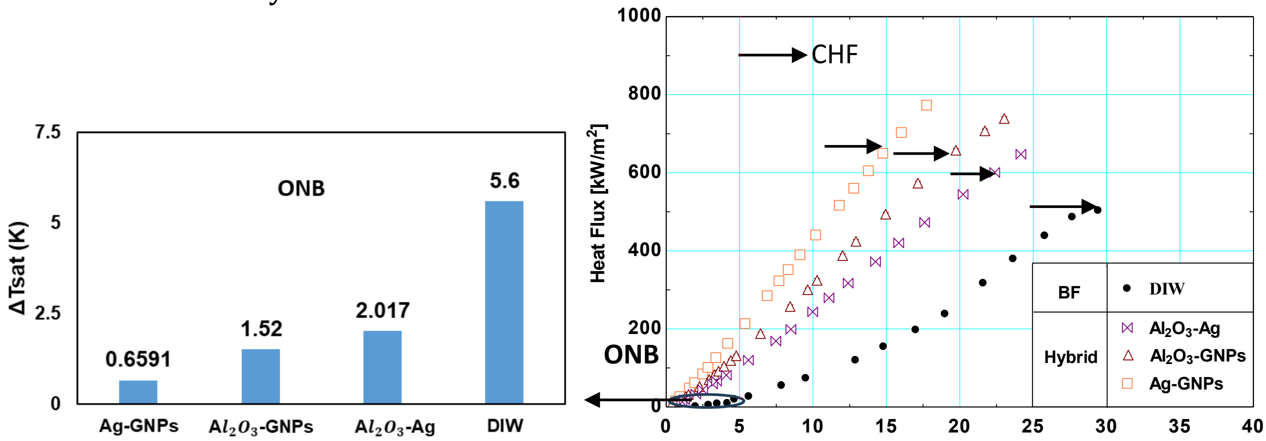

(A)

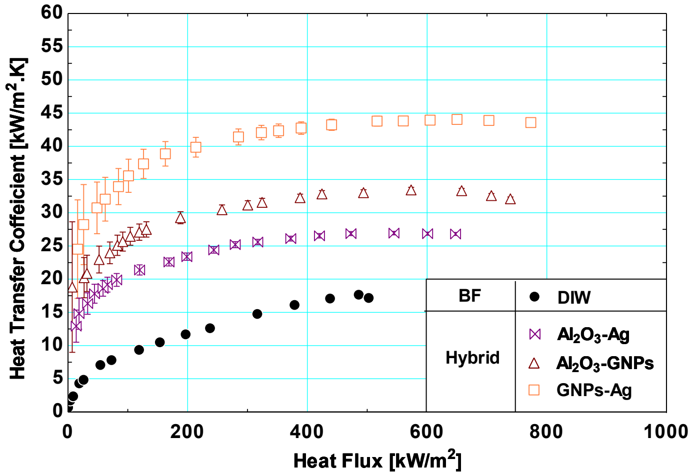

(B)

Figure 11. (A) Boiling curves and onset of nucleate boiling, and (B) Heat transfer coefficient curves of hybrid NFs compared with deionized water.

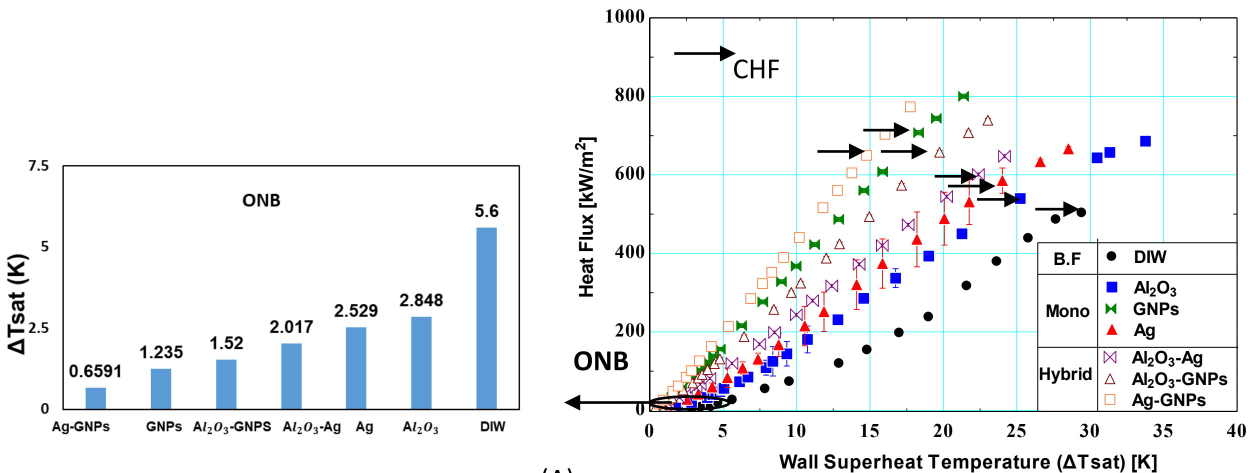

(A)

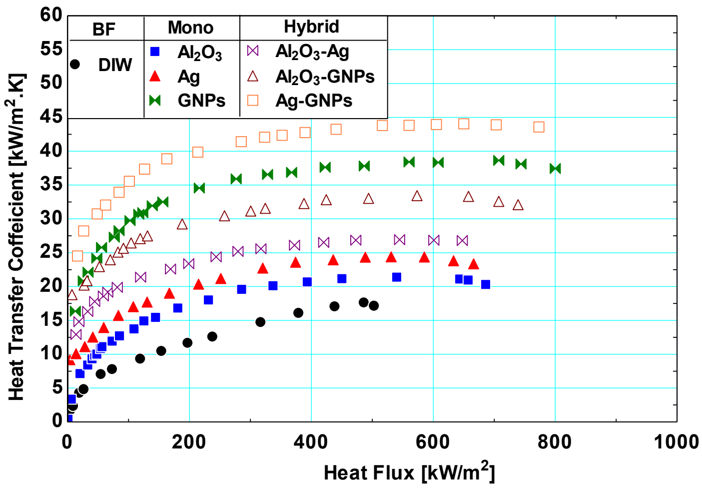

(B)

Figure 12. (A) Boiling curves and onset of nucleate boiling, and (B)Heat transfer coefficient curves of mono and hybrid NFs compared with deionized water.

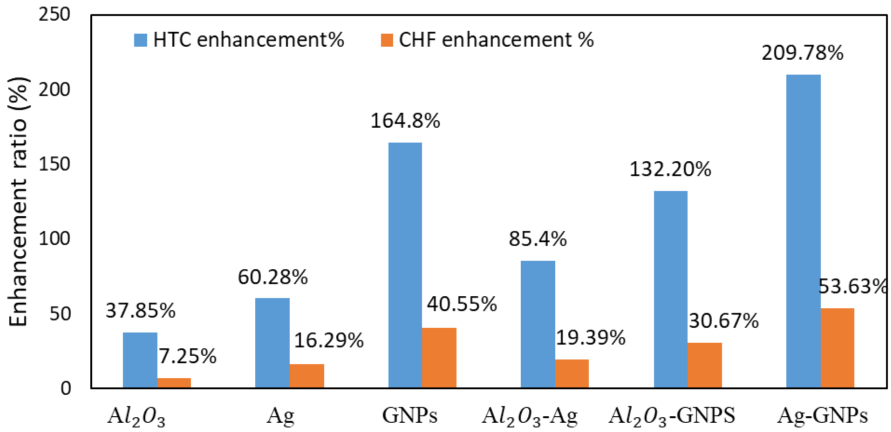

Figure 13. Enhancement ratio of the CHF and HTC for mono and hybrid NFs compared to the DIW.

4.3 Analysis of the Heat Transfer Mechanism of Nanofluids

4.3.1 Analysis of the Nanofluids Deposition Features

The heating surface's macroscopic morphology before and after the boiling of mono- and hybrid NFs is manifested in **Fig. 14.** The deposition depends strongly on the nanoparticle type, as confirmed by XRD and EDS. Post-boiling XRD patterns, as shown in **Fig. 15**, are dominated by FCC Cu reflections [(111), (200), (220), (311), (222)], indicating the preserved substrate crystallinity, though the peak intensity variations suggest surface microstructure modification. A critical observation is the appearance of a (002) reflection in all samples containing GNPs. This peak identifies the graphitic carbon ordering, confirming that the platelets are effectively anchored to the surface. Notably, for the mono-Ag, Al_2O_3, and hybrid Al_2O_3-Ag samples, the specific nanoparticle reflections are absent or negligible, indicating that these deposits form as thin, weakly crystalline, or partially amorphous layers. To identify the elemental composition of deposition nanoparticles, the Energy Dispersive Spectroscopy (EDS) analysis was used, as exhibited in **Fig. 16**. The EDS reveals that, for the mono Al_2O_3

and Ag samples, the deposition of Al and Ag was 8.8 wt% and 0.5 wt%, respectively, confirming thin or partial coatings. Also, the GNP sample exhibits a significantly lower oxygen concentration (1.8 wt%) than the mono Al_2O_3 and Ag samples (7.4 wt% and 2.9 wt%, respectively). This suggests that the GNPs form a graphitic, carbon-rich layer, which is a protective "carpet" that inhibits the formation of copper oxides, maintaining a more thermally conductive path between the heater and the fluid, yielding an improvement in the HTC. It should be noted that for the Al_2O_3 /DIW sample, part of the detected oxygen originates from the Al_2O_3 nanoparticles themselves (stoichiometrically ~47 wt% O) rather than exclusively from copper oxide formation, and EDS alone cannot distinguish between these two oxygen sources. Correcting for the oxygen contribution intrinsic to the deposited Al_2O_3 (estimated from the measured Al content) yields a CuOx-attributable oxygen value of 2.22 wt% for Al_2O_3 /DIW, compared with 2.9 wt% for Ag/DIW and 1.8 wt% for GNPs/DIW. This demonstrates that Al_2O_3 alone does not promote greater copper oxidation than Ag alone once its intrinsic oxygen contribution is accounted for, while the GNP-containing deposit retains the lowest oxidation, consistent with its role as an effective passivation layer against substrate oxidation. Consequently, the superior HTC and CHF observed in the GNP system are the results of a synergistic effect, as seen in **Figs. 10 A and B**.

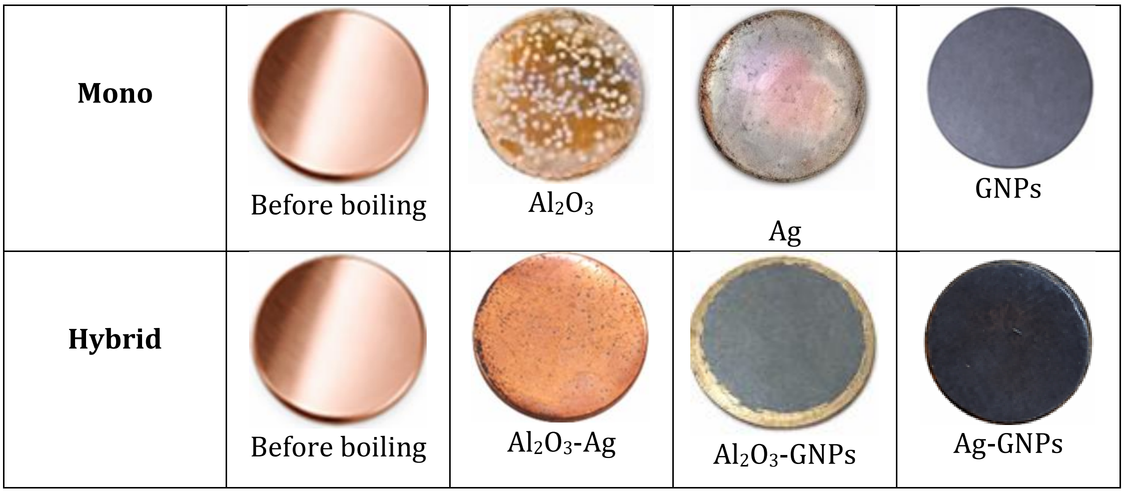

Figure 14. Morphology of nanoparticles deposition on surfaces before and after boiling

The EDS analysis of the hybrid deposits, as shown in **Fig. 16,** evinces a fundamental divergence in their chemical stability. Because Al_2O_3 itself is stoichiometrically oxygen-rich (~47 wt% O), the raw oxygen signal in Al_2O_3 -containing hybrids cannot be attributed solely to copper oxide formation; the oxygen intrinsic to the deposited Al_2O_3 was therefore subtracted (estimated from the measured Al content) to obtain the CuOx-attributable oxygen for each hybrid. On this corrected basis, the oxygen content was 1.7 wt% for Ag-GNPs, 1.56 wt% for Al_2O_3 -Ag, and 1.053 wt% for Al_2O_3 -GNPs. This indicates that, contrary to the trend suggested by the uncorrected values, the Al_2O_3 -Ag hybrid does not exhibit greater copper oxidation than Ag-GNPs; rather, the Al_2O_3 -GNPs hybrid shows the lowest CuOx-attributable oxygen among all three hybrid systems. This confirms that Graphene Nanoplatelets (GNPs) serve as a high-integrity protective barrier, passivating the copper substrate and suppressing the aggressive oxidation typically induced by pool-boiling conditions, and that this passivating effect is present whether GNPs are combined with Ag or with Al_2O_3. Consequently, the Ag-GNPs hybrid exhibits the highest HTC among the hybrid formulations, as evinced in **Fig. 11 B**, which is attributable primarily to its favorable surface characteristics

rather than to the lowest degree of copper oxidation, since the Al_2O_3 -GNPs hybrid shows even lower CuOx-attributable oxygen despite its lower HTC relative to Ag-GNPs.
However, adding a secondary phase can compromise the graphene's antioxidant effect. Ag-GNPs maintain a near-baseline oxygen level, but Al_2O_3-GNPs manifest elevated oxygen, indicating copper oxide formation. This oxide crust increases the wall superheat and, together with pore clogging by alumina, reduces the HTC, as illustrated in Fig. 15. Thus, minimizing the surface oxidation is essential for maximizing the boiling efficiency.
To further investigate the microstructural characteristics of the deposited layer formed by Al_2O_3, Ag, and GNPs nanoparticles, the SEM analysis was performed, as depicted in **Fig. 17**. The SEM images provide a detailed insight into the surface morphology, revealing significant variations in the coating uniformity depending on the nanoparticle type. Also, a microporous structure and more protrusions are found in the deposition layer and are well known to promote capillary effects and increase the nucleation sites and the HT area, thus enhancing HT performance. Furthermore, this microstructure may offer a plausible explanation for the behavior observed in the boiling curve shown in **Fig. 12A**. These structures act as potential nucleation sites for vapor and increase the effective nucleation site density. Accordingly, the nucleation sites density can be estimated as reported by **(Wang and Dhir, 1993)**:

$$N_a = 7.81 \times 10^{-29}(1 - \cos\theta)R_c^{-6} \quad (10)$$

Where, θ is the angle of contact, and Rc is the cavity radius, which was evaluated employing the **(Griffith and Wallis, 1958)**:

$$R_c = \frac{2\sigma T_{sat}}{(T_w - T_{sat})\rho_v h_{fg}} \quad (11)$$

The results of the cavity radius as a function of HF for the surfaces/WF (either DIW or NFs (mono/hybrid)) after boiling are shown on **Fig. 18**. In general, one may observe that the cavity radius of the surface nanoparticle deposition is larger in comparison with the surface boiling with the DIW. This observation indicates that a larger cavity radius requires less energy (i.e., lower wall superheat temperature) to activate the cavity. Thus, for a similar HF, a lower wall superheating was performed with an HNF (Ag-GNPs). However, at the higher HFs, an increased deposition rate caused the cavities to be filled with nanoparticles; therefore, resulting in a higher wall superheating for maintaining the cavities having active, smaller entrance diameters, which implies a lower HTC. **Fig. 19** portrays the effective nucleation sites density in terms of q'' for the surfaces/WF (either DIW or NFs (mono/hybrid)) after the boiling. It's obvious from this figure that boiling the surfaces with DIW yields more effective nucleation sites than boiling with F. This trend contrasts with that observed in **Fig. 12A** for the DIW, where the surface boiling with the DIW possessed the lowest HTC, i.e. the maximum wall superheating. Via the comparison of the HTC curves in **Fig. 12A** with the cavity radius and the effective nucleation sites number forecast and presented in **Figs. 18 and 19**, respectively, one may conclude about the prevailing influences upon the HTC as: The cavity radius appears to take a further significant part upon the conduct of HT, as for the similar q'', the bigger radii of cavity need less energy (i.e., smaller wall superheating) to be triggered, and such inference maintains the elevated HTC values stated in the present investigation. Thus, this agrees with the **(Manetti et al., 2017)** results, and the effective nucleation sites number isn't the prevailing influence upon the curves of HTC for the NFs. This behavior indicates that the cavity radius plays a crucial part in the boiling HT more than the nucleation site density.

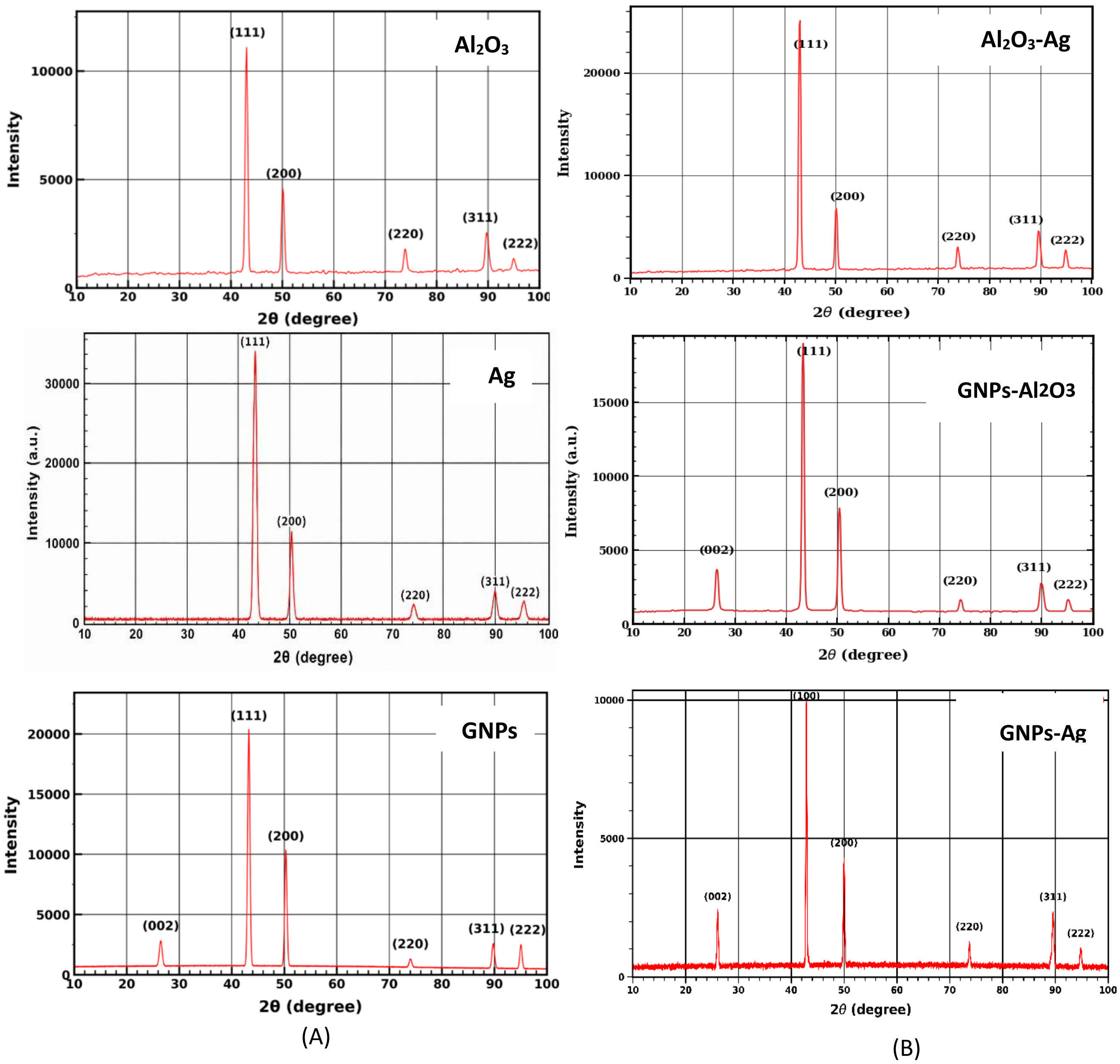

Figure 15. Patterns of the XRD for(A) Mono NFs and (B) Hybrid NFs.

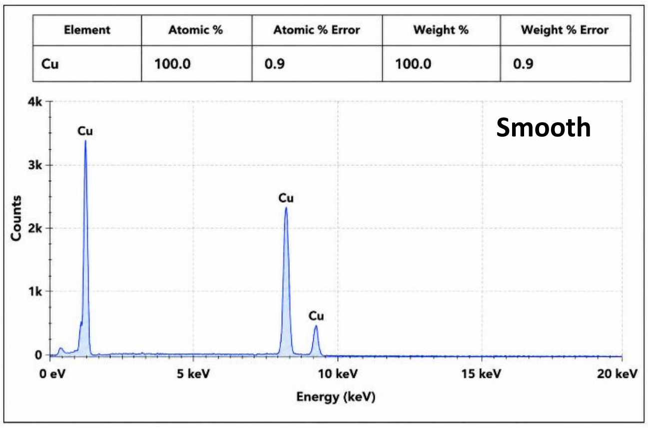

Element	Atomic %	Atomic % Error	Weight %	Weight % Error
Cu	100.0	0.9	100.0	0.9

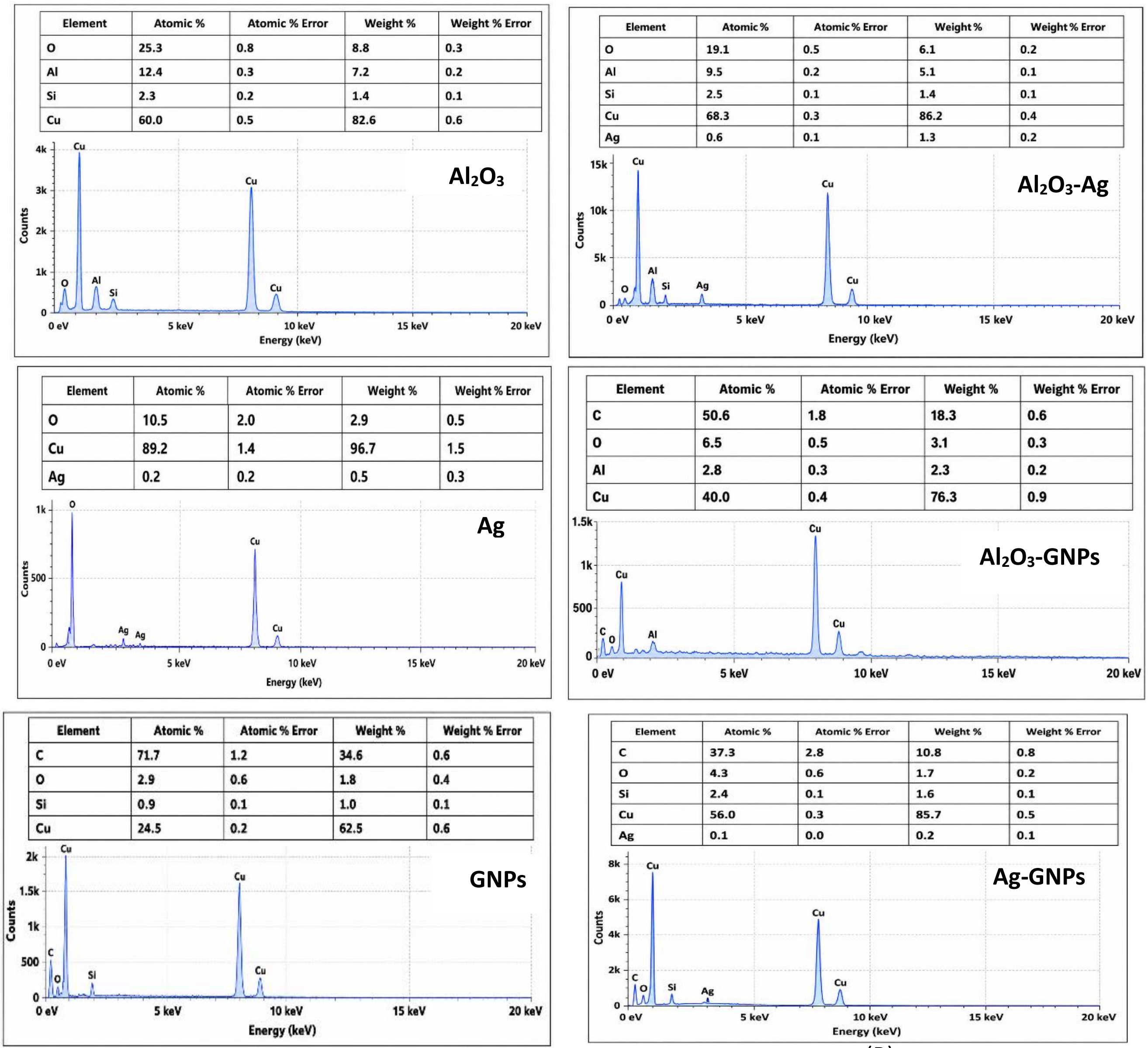

Element	Atomic %	Atomic % Error	Weight %	Weight % Error
O	25.3	0.8	8.8	0.3
Al	12.4	0.3	7.2	0.2
Si	2.3	0.2	1.4	0.1
Cu	60.0	0.5	82.6	0.6

Element	Atomic %	Atomic % Error	Weight %	Weight % Error
O	19.1	0.5	6.1	0.2
Al	9.5	0.2	5.1	0.1
Si	2.5	0.1	1.4	0.1
Cu	68.3	0.3	86.2	0.4
Ag	0.6	0.1	1.3	0.2

Element	Atomic %	Atomic % Error	Weight %	Weight % Error
O	10.5	2.0	2.9	0.5
Cu	89.2	1.4	96.7	1.5
Ag	0.2	0.2	0.5	0.3

Element	Atomic %	Atomic % Error	Weight %	Weight % Error
C	50.6	1.8	18.3	0.6
O	6.5	0.5	3.1	0.3
Al	2.8	0.3	2.3	0.2
Cu	40.0	0.4	76.3	0.9

Element	Atomic %	Atomic % Error	Weight %	Weight % Error
C	71.7	1.2	34.6	0.6
O	2.9	0.6	1.8	0.4
Si	0.9	0.1	1.0	0.1
Cu	24.5	0.2	62.5	0.6

Element	Atomic %	Atomic % Error	Weight %	Weight % Error
C	37.3	2.8	10.8	0.8
O	4.3	0.6	1.7	0.2
Si	2.4	0.1	1.6	0.1
Cu	56.0	0.3	85.7	0.5
Ag	0.1	0.0	0.2	0.1

(A) (B)

Figure 16. Energy Dispersive X-ray spectroscopy (EDS) measurement of (A) Mono and (B) Hybrid nanofluid**.**

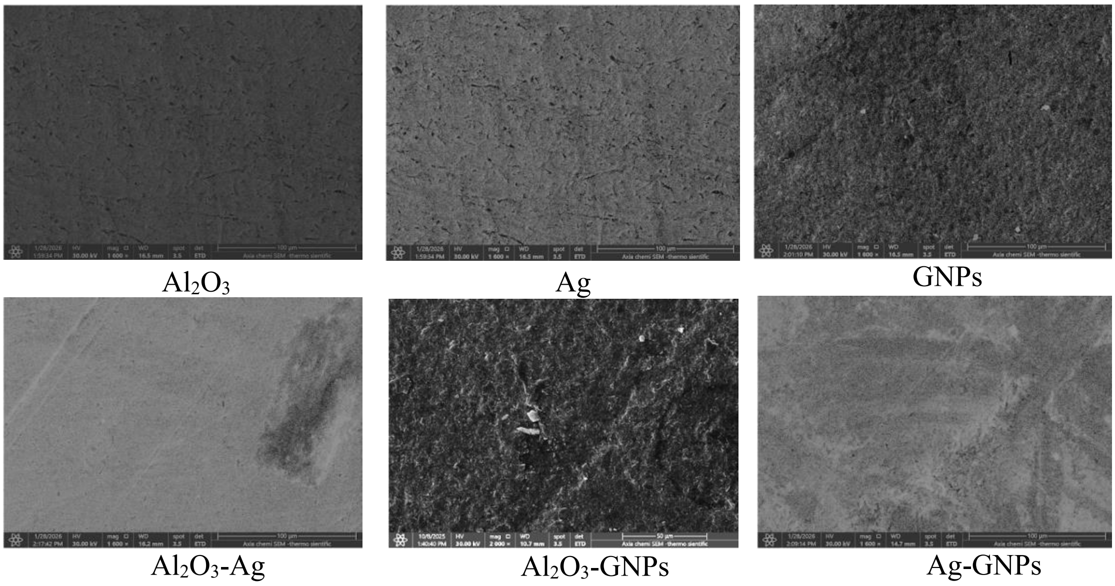

Figure 17. Scanning electron microscope image of the heating test surface before and after boiling.

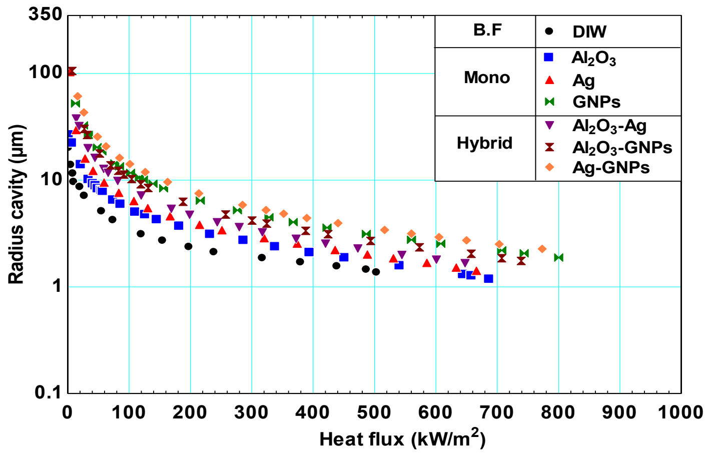

Figure 18. Influence of the heat flux and the surface WF upon the radius of the cavity.

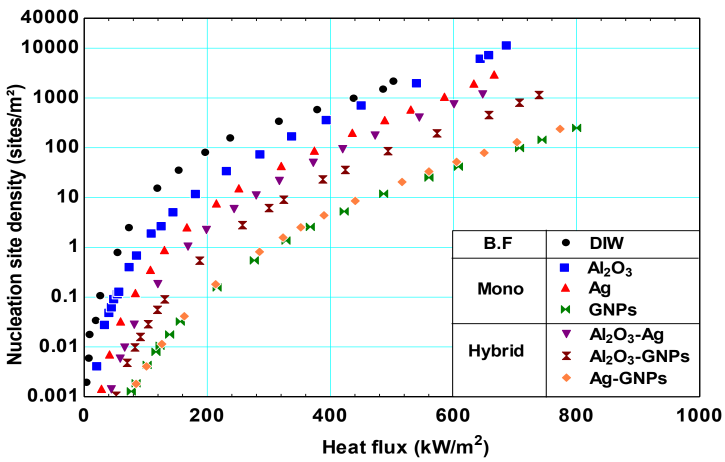

Figure 19. Influence of the heat flux and the surface WF upon the effective nucleation site density.

4.3.2 Effect of the Heating Surface Wettability upon the Boiling Heat Transfer

Nanoparticle deposition alters the wettability of the boiling surface. The smooth, unmodified copper surface exhibited an initial contact angle of 62.21° (hydrophilic). After boiling of the MNFs, the contact angle increased to 90° for Al_2O_3/DIW, 80.5° for Ag/DIW, and decreased slightly to 56.5° for GNPs/DIW, as shown in **Fig. 20**. Among these, the Al_2O_3/DIW deposit produced the largest shift toward hydrophobicity, approaching the 90° threshold, while the GNPs/DIW deposit remained the most hydrophilic. Furthermore, for the HNFs, the surface contact angle exhibited different trends depending on the composition, increasing to 83.46° and 95° (hydrophobic) for Al_2O_3-Ag/DIW and Al_2O_3-GNPs/DIW, respectively, and decreasing to 67.07° (hydrophilic) for Ag-GNPs/DIW, relative to the 62.21° smooth-surface baseline. Generally, hydrophobic surfaces tend to promote the formation of bubbles at a lower wall superheat and to activate the nucleation sites, thereby enhancing the HTC. Conversely, the hydrophilic surfaces operated to rewet the heated test surface and spread the fluid, which slows the development of a vapour blanket and, consequently, promotes the CHF, **(Quan, Wang and Cheng, 2017)**. These results indicated that the HNF composed of Ag-GNPs observed an important improvement in CHF in comparison with the mono and hybrid NFs due to the hydrophilicity. However, this contrasts with the remark that the Al_2O_3-GNPs HNF, which has a contact angle greater than 95° (hydrophobic), exhibits a greater HT performance enhancement than Al_2O_3-Ag at 83.46°. This phenomenon can be explained as follows: According to the SEM image in this study and the aforementioned discussion in Section 4.3.1, the microporous structure promotes capillary effects, thereby improving CHF. So, the deposition surface porosity after boiling the mono and hybrid NFs was calculated from the SEM images using Image-J software, as demonstrated in **Fig. 21**.

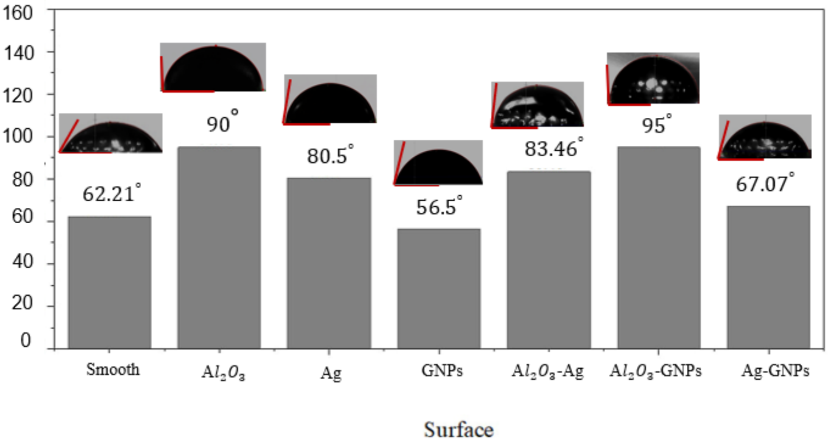

Figure 20. The deionized water contact angle images upon the smooth Cu surface and the deposition of nanoparticle surfaces.

One can observe in this figure that the Ag-GNPs deposited layer exhibited the highest porosity among all mono and hybrid nanofluids investigated, reaching approximately 36.5%, compared with 33.54% for Al_2O_3-GNPs and 23.20% for Al_2O_3-Ag. This elevated porosity is consistent with the superior CHF performance of the Ag-GNPs hybrid, which achieved the highest CHF enhancement among all tested fluids. This enhancement is attributed not only to the relative hydrophilicity of the Ag-GNPs surface, reflected in its reduced contact angle of 67.07°, but also to its highly porous deposited structure. Together, these two properties induce a capillary wicking effect that supplies more fresh liquid to the vapor–liquid interface, efficiently delaying surface dry-out and thereby raising the CHF, consistent with the mechanism reported by **(Ma et al., 2022)**. These results indicate that wettability alone is insufficient to enhance boiling performance and that deposited-layer porosity plays an equally critical role in governing CHF enhancement.

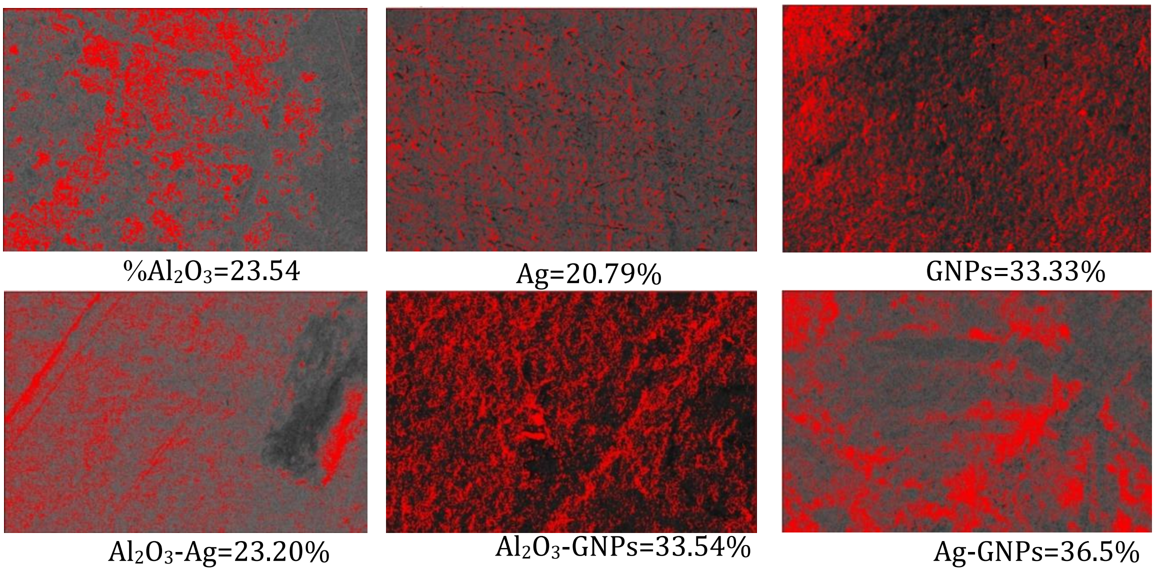

Figure 21. Porosity of the heating testing surface after boiling the NF (by SEM integrated with Image-J software).

4.3.3 Influence of Heating Surface Roughness upon the Boiling HT

Atomic force microscopy (AFM) was used to examine the samples' surface morphology and characterize the surface roughness before and after boiling the mono and hybrid NFs, as shown in **Fig. 22**. The results indicate that heating the copper surface before the boiling exhibits considerably lower surface roughness compared to that with the deposited nanoparticles following the boiling process. Generally, individual nanoparticle deposition increases the heated surface roughness, thereby increasing the density of effective nucleation sites and improving HT performance. This trend was consistently observed for the surfaces modified with Al_2O_3 and GNPs, where the increased roughness and the augmented nucleation sites number corresponded to the enhanced HTC. However, the silver (Ag) nanoparticles deviated from this pattern, displaying a relatively lower surface roughness. Despite this, the Ag/DIW NF exhibited superior HT relative to Al_2O_3 NFs, which can be ascribed to the inherently higher TC of silver. For the HNFs, the Ag-GNP composition exhibited higher surface roughness, resulting in a superior HTC compared with the other HNF compositions. Although the Al_2O_3-Ag HNF had a higher surface roughness than the Al_2O_3-GNPs NF, its HTC was lower. This behavior could be ascribed to the elevated TC of GNPs. And, the analysis of EDS, as portrayed in the **Fig. 16**, confirms this by indicating that the GNPs content in the Al_2O_3-GNPs HNF reaches approximately 18.3%. This paradox is attributed to the deposition of spherical Al_2O_3 and Ag nanoparticles that fill the pores among the GNPs, creating a dense, highly effective roughness layer.

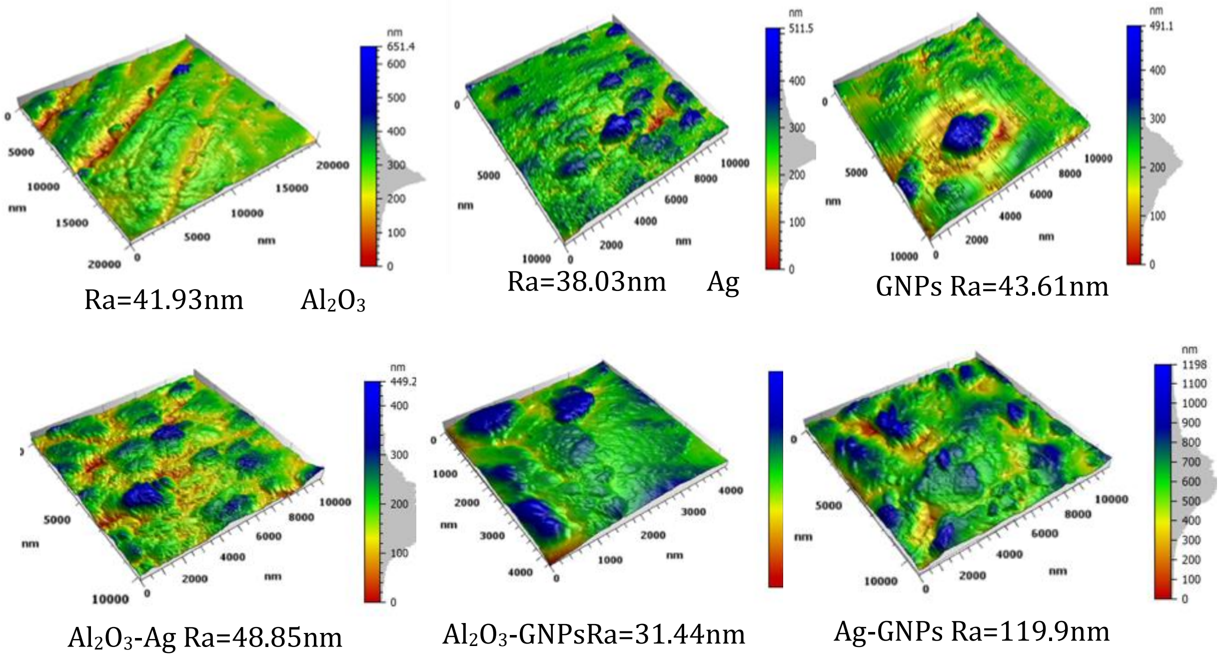

Figure 22. The 3-D view of surface roughness analysis of the heating testing surface before and after boiling the NF.

5. CONCLUSIONS

This study investigated the saturated pool boiling performance of low-concentration (0.01 vol%) mono- and hybrid nanofluids (Al_2O_3, Ag, GNPs, Ag-GNPs, Al_2O_3-GNPs, and Al_2O_3-Ag) on a smooth copper surface. Boiling measurements and post boiling surface characterization showed that cavity radius, deposit porosity, and oxidation resistance govern boiling enhancement more strongly than nucleation-site density or wettability alone. The main findings are:

1. All nanofluids reduced the wall superheat at the onset of nucleate boiling (ONB), with Ag-GNPs showing the largest reduction of 88.23%.
2. Mono GNPs outperformed Al_2O_3-containing nanofluids, achieving CHF and HTC enhancements of 40.55% and 164.8%, respectively, compared with 30.67% and 132.2% for Al_2O_3-GNPs. This indicates that adding Al_2O_3 to GNPs reduces HTC enhancement.
3. Ag-GNPs provided the best overall performance, with CHF and HTC enhancements of 53.63% and 209.8%. This improvement is attributed to a larger effective cavity radius, the high thermal conductivity of Ag, and the porous protective structure formed by GNPs.
4. The addition of Al_2O_3 to GNPs reduces performance relative to pure GNPs, but this is not due to increased copper oxidation. Instead, the reduced performance is attributed to Al_2O_3 physically occluding the microporous structure formed by GNPs, which lowers the effective cavity radius and HTC, although CHF remains high due to enhanced wettability and porosity.
5. Cavity radius was found to influence boiling performance more strongly than nucleation-site density, as larger cavities activate at lower wall superheat and enhance nucleation and HTC.
6. Wettability alone cannot explain the boiling enhancement. Porosity improves capillary wicking and delays dry-out, while the superior Ag-GNPs performance results from the combined effects of moderate hydrophilicity, favorable porous structure, and improved oxidation resistance.

NOMENCLATURE

Symbol	Description	Symbol	Description
H	Heat transfer coefficient (kW/m^2. K)	Na	Density of nucleation site ($site/m^2$)
h_{fg}	Latent Heat of Vaporization (J/kg)	θ	Contact angle, deg.
q''	Heat flux (kW/m^2)	ρ	Density, kg/m^3
Ts	Surface temperature (K)	σ	Surface tension, N/m
K	Thermal conductivity (W/m.K)	ΔT	Wall superheating, K
Rc	Radius of cavity (μm)		

Credit Authorship Contribution Statement

Rahma Sh. Kadhim: Conceptualization, Methodology, Validation, Writing-Original Draft, Data Curation. Ekhlas M. Fayyadh: Conceptualization, Validation, Administration, Writing-Review, Supervision. Qahtan A. Al-Nakeeb: Conceptualization, Validation, Administration, Supervision

Declaration of Competing Interest

The authors declare that they have no known competing financial interests or personal relationships that could have appeared to influence the work reported in this paper.

REFERENCES

Abid, B.A. and Getan, M.K., 2010. Heat transfer in pool boiling with surfactants. *Eng. & Tech. Journal*, 28(17), pp. 5421–5422.

Ajeeb, W. and Murshed, S.M.S., 2023. Pool boiling heat transfer characteristics of SiO_2 and BN nanoparticles dispersed mono and hybrid nanofluids. *Nanomaterials*, 13(19). https://doi.org/10.3390/nano13192625.

Akbari, A., Fazel, S.A.A., Maghsoodi, S., Kootenaei, A.S., 2019. Pool boiling heat transfer characteristics of graphene-based aqueous nanofluids. *Journal of Thermal Analysis and Calorimetry*, 135(1), pp. 697–711. https://doi.org/10.1007/s10973-018-7182-2.

Akhtar, A.M.Z., Rahman, M.M., Kadirgama, K., Saidur, R., Safiei, W., 2022. Effects of temperature and concentration on thermophysical properties of TiO_2-MWCNTs-doped graphene nanofluids. *Materials Today: Proceedings*, 48(January), pp. 920–925. https://doi.org/10.1016/j.matpr.2021.03.725

Ali, N., 2022. Graphene-based nanofluids : Production parameter effects on thermophysical properties and dispersion stability. *nanomaterials (MDPI)*, 12(357). https://doi.org/10.3390/nano12030357.

AlMuhaysh, K.A., Sergis, A. and Hardalupas, Y., 2025. Effects of pH and nanoparticle concentration on Al_2O_3–H_2O nanofluid stability. *International Journal of Thermophysics*. Springer US. https://doi.org/10.1007/s10765-025-03557-x

Al-obaidy, A.M.H., Fayyadh, E.M. and Al-dabagh, A.M., 2024. Effect of the geometrical parameter of open microchannel on pool boiling enhancement. *Engineering and Technology Journal*, 42(07), pp. 1–22. https://doi.org/10.32604/fhmt.2024.055063.

Anderson, D. A., Tannehill, J.C., Pletcher, R.H., Munipalli, R., Shankar, V., 1984. *Computational Fluid Mechanics and Heat Transfer*. 4th edn. Hemisphere Publishing Corporation.

Borode, A., Tshephe, T. and Olubambi, P., 2023. Stability and thermophysical properties of GNP-Fe_2O_3

hybrid nanofluid : Effect of volume fraction and temperature. *nanomaterials*, 13(1238). https://doi.org/10.3390/nano13071238.

Coleman, H.W., and Steck, W.G.J., 1989 *Experimentation and Uncertainty Analysis for Engineers*. New York: John Wiley and Sons, Inc.

Cooper, M.G., 1984. Heat flow rates in saturated nucleate pool boiling-a wide-ranging examination using reduced properties. *Advances in heat transfer*, 16, pp. 157-239. Elsevier. https://doi.org/10.1016/S0065-2717(08)70205-3

Cornwell, K. and Houston, S.D., 1994. Nucleate pool boiling on horizontal tubes : A convection- based correlation. *International Journal of Heat and Mass Transfer*, 37, pp. 303–309. https://doi.org/10.1016/0017-9310(94)90031-0

Du, J., Wang, Y., Yang, W., Wang, J., Cao, Z., and Sundén, B., 2024. Effect of nanoparticle concentration and surfactants on nanofluid pool boiling. *International Journal of Heat and Mass Transfer*, 221(125080). https://doi.org/10.1016/j.ijheatmasstransfer.2023.125080

Du, J., Yang, W., Zhu, H., Wang, J., Cao, Z., and Sundén, B., 2024. Experimental study of pool boiling performance of Fe_3O_4 ferromagnetic nanofluid on a copper surface. *Applied Thermal Engineering*, 248. https://doi.org/10.1016/j.applthermaleng.2024.123213

Ebrahim, S.A., Pradeep, E., Mukherjee, S., and Ali, N., 2023. Rheological behavior of dilute graphene-water nanofluids using various surfactants : An experimental evaluation. *Journal of Molecular Liquids*, 370, P. 120987. https://doi.org/10.1016/j.molliq.2022.120987

Gao, Y. XI, Y., Yang, Z., Sasmito, A.P., Mujumdar, S.A., and Wang, L., 2021. Experimental investigation of specific heat of aqueous graphene oxide Al_2O_3 hybrid nanofluid. *Thermal Science*, 25(1 Part B), pp. 515–525. https://doi.org/10.2298/TSCI190404381G

Golkar, S.H., Khayat, M. and Zareh, M., 2021. Experimental study of heat transfer characteristics of nanofluid nucleate and film boiling on horizontal flat plate. *Scientia Iranica*, 28(6B), pp. 3216–3231. https://doi.org/10.24200/sci.2021.56967.4997

Griffith, P. and Wallis, J.D., 1958. The role of surface conditions in nucleate boiling. *Massachusetts Institute of Technology* [Preprint], (14).

Gupta, S.K. and Misra, R.D., 2023. Effect of novel Cu@ ZnO hybrid nanofluids on pool boiling heat transfer performance. *International Journal of Thermophysics*, 44(9), P. 134. https://doi.org/10.1007/s10765-023-03240-z

Holman, J.P., 2010. *Heat Transfer*. 10th edn. New York: McGraw-Hill.

Jalilov, D., Juraev, T., Halimov, A., and Akhatov, J., 2026. Stability enhancement of oxidized carbon black nanofluids: effects of concentration, sonication time, and SDS surfactant. *Heat and Mass Transfer*, 62(2), P. 9. https://doi.org/10.1007/s00231-025-03638-5

Ji, W., Zhao, C., He, Y., and Tao, W., 2015. Experimental validation of Cooper correlation at higher heat flux. *International Journal of Heat and Mass Transfer*, 90, pp. 1241–1243. https://doi.org/10.1016/j.ijheatmasstransfer.2015.05.107

Jones, B.J., McHale, J.P. and Garimella, S. V., 2009. The influence of surface roughness on nucleate pool boiling heat transfer. *Journal of Heat Transfer*, 131(12), pp.1–14. https://doi.org/10.1115/1.3220144

Jung, D., Lee, H., Bae, D., and Oho, S., 2004. Nucleate boiling heat transfer coefficients of flammable refrigerants. *International Journal of Refrigeration*, 27, pp. 409–414. https://doi.org/10.1016/j.ijrefrig.2003.11.007

Kamel, M.S. and Lezsovits, F., 2020. Enhancement of pool boiling heat transfer performance using dilute cerium oxide/water nanofluid: An experimental investigation. *International Communications in Heat and Mass Transfer*, 114(April), P. 104587. https://doi.org/10.1016/j.icheatmasstransfer.2020.104587

Kamel, M.S., and Lezsovits, F., 2020. Experimental investigation on pool boiling heat transfer performance using Tungsten Oxide WO_3 nanomaterial-basedwater nanofluids. *Materials*, 13(1922). https://doi.org/10.3390/ma13081922

Kamel, M.S., Lezsovits, F., Abdollah, A., and Izadi, M., 2021. Amelioration of pool boiling thermal performance in case of using a new hybrid nanofluid. *Case Studies in Thermal Engineering*, 24, P. 100872. https://doi.org/10.1016/j.csite.2021.100872

Karikalan, L., Poyyamozhi, B.N., and Negash, K., 2022. Experimental analysis of heat transfer by using nanofluid and impact of thermophysical properties. *Journal of Nanomaterials*, 2022(1), P. 5119797. https://doi.org/10.1155/2022/5119797

Kwark, S.M., Kumar, R., Moreno, G., Yoo, J., and You, S., 2010. Pool boiling characteristics of low concentration nanofluids. *International Journal of Heat and Mass Transfer*, 53(5–6), pp. 972–981. https://doi.org/10.1016/j.ijheatmasstransfer.2009.11.018

Li, Y., Chen, Y. and Liu, Z., 2014. A uniform correlation for predicting pool boiling heat transfer on plane surface with surface characteristics effect. *International Journal of Heat and Mass Transfer*, 77, pp. 809–817. https://doi.org/10.1016/j.ijheatmasstransfer.2014.05.060

Li, Z. Asadi, S., Karimipour, A., Abdollahi, A., and Tlili, I., 2020. Experimental study of temperature and mass fraction effects on thermal conductivity and dynamic viscosity of SiO_2-oleic acid/liquid paraffin nanofluid. *International Communications in Heat, and Mass Transfer*, 110. https://doi.org/10.1016/j.icheatmasstransfer.2019.104436

Ma, X., Song, Y., Wang, Y., Zhang, Y., Xu, J., Yao, S. and Vafai, K., 2022. Experimental study of boiling heat transfer for a novel type of GNP-Fe_3O_4 hybrid nanofluids blended with different nanoparticles. *Powder Technology*, 396, pp. 92–112. https://doi.org/10.1016/j.powtec.2021.10.029

Maheshwary, P.B., Handa, C.C., Nemade, K.R., and Chaudhary, S.R., 2020. Role of nanoparticle shape in enhancing the thermal conductivity of nanofluids. *Materials Today: Proceedings*, 28, pp. 873–878. https://doi.org/10.1016/j.matpr.2019.12.315

Manetti, L.L., Stephen, M.T., Beck, P.A., and Cardoso, E.M., 2017. Evaluation of the heat transfer enhancement during pool boiling using low concentrations of Al_2O_3-water based nanofluid. *Experimental Thermal and Fluid Science*, 87, pp. 191–200. https://doi.org/10.1016/j.expthermflusci.2017.04.018.

Mehralizadeh, A., Shabanian, S.R. and Bakeri, G., 2020. Experimental and modeling study of heat transfer enhancement of TiO_2/SiO_2 hybrid nanofluids on modified surfaces in pool boiling process. *European Physical Journal Plus*, 135(10). https://doi.org/10.1140/epjp/s13360-020-00809-7

Mehralizadeh, A., Shabanian, S.R., and Bakeri, G., 2020. Effect of modified surfaces on bubble dynamics and pool boiling heat transfer enhancement: A review. *Thermal Science and Engineering Progress*, 15, P. 100451. https://doi.org/10.1016/j.tsep.2019.100451

Mohamed, S.A., Elsherbini, A.M., Alrefaey, H.R., Adelrahman, K., Moustafa, A., Egodawaththa, N.M., Crawford, K.E., Nesnas, N. and Sabra, S.A., 2025. Gum Arabic: A commodity with versatile formulations and applications. Nanomaterials, 15(4), P. 290.. https://doi.org/10.3390/nano15040290

Moldoveanu, G.M., Ibanescu, C. and Minea, A.A., 2018. Viscosity estimation of Al_2O_3, SiO_2 nanofluids and their hybrid: An experimental study Georgiana. *Journal of Molecular Liquids* [Preprint]. https://doi.org/10.1016/j.molliq.2018.01.061%20MOLLIQ

Mostafizur, R.M., Rasul, M.G. and Nabi, M.N., 2022. Effect of surfactant on stability , thermal conductivity , and viscosity of aluminium oxide – methanol nanofluids for heat transfer applications. *Thermal Science and Engineering Progress*, 31(April), P. 101302. https://doi.org/10.1016/j.tsep.2022.101302

Mousavi, S.M., Esmaeilzadeh, F. and Wang, X.P., 2019. A detailed investigation on the thermo-physical and rheological behavior of MgO/TiO_2 aqueous dual hybrid nanofluid, 282, pp. 323–339. https://doi.org/10.1016/j.molliq.2019.02.100

Mukherjee, S., Mishra, P.C. and Chaudhuri, P., 2021. Pool boiling performance of aqueous Al_2O_3 and TiO_2 nanofluids on a horizontally placed flat polished surface: an experimental investigation. *Journal of Thermal Analysis and Calorimetry*, 146(1), pp. 415–433. https://doi.org/10.1007/s10973-020-09995-z.

Nazir, A., Qamar, A., Rafique, M.S., Murtaza, G., Arshad, T., Muneeb, A., Jabeen, K., Mujtaba, M.A., Fayaz, H. and Saleel, C.A., 2024. Enhanced thermal conductivity of plasma generated ZnO–MgO based hybrid nanofluids: An experimental study. *Heliyon*, 10(4), p. 26396. https://doi.org/10.1016/j.heliyon.2024.e26396

Parwin, S., Parui, J., 2020. Ag nanofluids synthesis in presence of citrate at different stirring rotation and their post reaction stability. *Journal of Dispersion Science and Technology.* https://doi.org/10.1080/01932691.2020.1789469

Pioro, I.L., Rohseno. w., Doerffer, S.S., 2004. Nucleate pool-boiling heat transfer. I: review ofparametric effects of boiling surface. *International Journal of Heat and Mass Transfer*, 47(23), pp. 5033–5044. https://doi.org/10.1016/j.ijheatmasstransfer.2004.06.019

Quan, X., Wang, D. and Cheng, P., 2017. An experimental investigation on wettability effects of nanoparticles in pool boiling of a nanofluid. *International Journal of Heat and Mass Transfer*, 108, pp. 32–40. https://doi.org/10.1016/j.ijheatmasstransfer.2016.11.098

Reddy, Y.A. and Venkatachalapathy, S., 2018. Heat transfer enhancement studies in pool boiling using hybrid nanofluids. *Thermochimica Acta*, P. 27. https://doi.org/10.1016/j.tca.2018.11.014

Saha, G., 2016. *Heat Transfer Performance Investigation of Nanofluids Flow in Pipe*. University of Glasgow. https://gla.on.worldcat.org/oclc/1547493087

Sarafraz, M.M., Pourmehran, O., Yang, B., Yang, M., and Arjomandi, R., 2020. Pool boiling heat transfer characteristics of iron oxide nano-suspension under constant magnetic field. *International Journal of Thermal Sciences*, 147(May 2018), P. 106131. https://doi.org/10.1016/j.ijthermalsci.2019.106131

Selvarajoo, K., Wanatasanappan, V.V., and Luon, N.Y., 2024. Experimental measurement of thermal conductivity and viscosity of Al_2O_3-GO (80:20) hybrid and mono nanofluids : A new correlation. *SSRN*, 144(111018), P. 21. https://doi.org/10.1016/j.diamond.2024.111018

Sezer, N., Khan, S.A. and Koç, M., 2020. Boiling heat transfer enhancement by self-assembled graphene/silver hybrid film for the thermal management of concentrated photovoltaics. *Energy Technology*, 8(11), pp. 1–14. https://doi.org/10.1002/ente.202000532

Shaik, A.H., Chakraborty, S., Saboor, S., Kumar, K.R., Majumdar, A., Rizwan, M., Arıcı, M. and Chandan, M.R., 2024. Cu-Graphene water-based hybrid nanofluids: Synthesis, stability, thermophysical characterization, and figure of merit analysis. *Journal of Thermal Analysis and Calorimetry*, 149(7), pp. 2953–2968. https://doi.org/10.1007/s10973-023-12875-x.

Sharma, P.O. and Unune, D.R., 2023. Amelioration of pool boiling performance using hybrid nanofluids over EDMed surfaces. *Journal of Thermal Analysis and Calorimetry*, 148(6), pp. 2657–2676. https://doi.org/10.1007/s10973-022-11922-3.

Sharma, P.O., Barewar, S.D. and Chougule, S.S., 2021. Experimental investigation of heat transfer enhancement in pool boiling using novel Ag/ZnO hybrid nanofluids. *Journal of Thermal Analysis and Calorimetry*, 143(2), pp. 1051–1061. https://doi.org/10.1007/s10973-020-09922-2

Tiwari, A.K., Pandya, N.S., Shah, H., and Said, Z., 2020. Experimental comparison of specific heat capacity of three different metal oxides with MWCNT / water - based hybrid nanofluids : Proposing a new correlation. *Applied Nanoscience* [Preprint]. https://doi.org/10.1007/s13204-020-01578-6

Vafaei, S., 2015. Nanofluid pool boiling heat transfer phenomenon. *Powder Technology*, 277, pp. 181–192. https://doi.org/10.1016/j.powtec.2015.02.040

Vajjha, R.S. and Das, D.K., 2009. Experimental determination of thermal conductivity of three nanofluids and development of new correlations. *International Journal of Heat and Mass Transfer*, 52(21–22), pp. 4675–4682. https://doi.org/10.1016/j.ijheatmasstransfer.2009.06.027

Vicki, W. V, Abdullah, M.Z., and Gunnasegaran, P., 2020. Thermophysical properties of Al_2O_3-CuO hybrid nanofluid at different nanoparticle mixture ratio: An experimental approach. *Journal of Molecular Liquids*, P. 113458. https://doi.org/10.1016/j.molliq.2020.113458

Wang, C.H. and Dhir, V.K., 1993. On the gas entrapment and nucleation site density during pool boiling of saturated water. *Heat and Mass Transfer*, 115(3), pp. 670–679. https://doi.org/10.1115/1.2910738

Wen, T., Luo,J., Jiao, K., and Lu, L., 2023. Experimental study on the pool boiling performance of a highly self-dispersion TiO_2 nanofluid on copper surface. *International Journal of Thermal Sciences*, 184, P. 107999. https://doi.org/10.1016/j.ijthermalsci.2022.107999

Xiao, L., Zhuang, Y., Wu, X., Yang, J., Lu, Y., Liu, Y. and Han, X., 2023. A review of pool-boiling processes based on bubble-dynamics parameters. *Applied Sciences (Switzerland)*, 13(21). https://doi.org/10.3390/app132112026

You, S.M., Kim, J.H. and Kim, K.H., 2003. Effect of nanoparticles on critical heat flux of water in pool boiling heat transfer. *Applied Physics Letters*, 83(16), pp. 3374–3376. https://doi.org/10.1063/1.1619206

التأثيرات التآزرية والتضادية لترسّب الجسيمات النانوية في الموائع النانوية الأحادية والهجينة منخفضة التركيز على انتقال الحرارة بالغليان الحوضي

رحمة شكري كاظم*، اخلاص محمد فياض، قحطان عباس النقيب

كلية الهندسة الميكانيكية, الجامعة التكنولوجية, بغداد, العراق

الخلاصة

إنَّ التزايد المســتمر في متطلبات تبديد الحرارة في الإلكترونيات الحديثة عالية الأداء يتطلب تقنيات تبريد متقدمة تتجاوز قدرات الموائع التقليدية، وقد برزت الموائع النانوية بوصفها خيارًا واعدًا لتعزيز انتقال الحرارة بالغليان. تهدف هذه الدراسة إلى التحقيق تجريبيًا في أداء الغليان البركي للموائع النانوية الأحادية والهجينة عند تركيز حجمي منخفض قدره 0.01% باستخدام الماء منزوع الأيونات (DIW) بوصفه السائل الأساس وسطح نحاسي أملس تحت ظروف الغليان المشبع. شملت الدراسة ثلاثة موائع نانوية أحادية (Al_2O_3/DIW، وAg/DIW، وGNPs/DIW) وثلاثة موائع نانوية هجينة بنسبة خلط ثابتة 50:50 هي (Al_2O_3–Ag/DIW، وAl_2O_3–GNPs/DIW، وAg–GNPs/DIW)، مع تقييم الفيض الحراري الحرج (CHF) ومعامل انتقال الحرارة (HTC).أظهرت جميع الموائع النانوية تحسـنًا في أداء الغليان مقارنةً بالماء منزوع الأيونات. ومن بين الموائع الأحادية، حقق GNPs/DIW أفضل أداء بزيادة بلغت 40.55% في الفيض الحراري الحرج و164.8% في معامل انتقال الحرارة. كما سجل المائع النانوي الهجين Ag–GNPs/DIW أعلى أداء إجمالًا، محققًا زيادة قدرها 53.63% في الفيض الحراري الحرج و209.8% في معامل انتقال الحرارة. في المقابل، أظهر المائع الهجين Al_2O_3–GNPs/DIW انخفاضًا في أداء انتقال الحرارة مقارنةً بـ GNPs/DIW نتيجة التأثيرات التضادية لترسب جسيمات Al_2O_3.وأوضحت تحليلات SEM وEDS وXRD وزاوية التلامس والمسامية أن ترسب صفائح الجرافين النانوية يُكوّن طبقة جرافيتية واقية تقلل أكسدة النحاس وتعزز مسامية السطح ونصف قطر تجاويف الغليان، مما يحسن انتقال الحرارة، في حين يعزز Al_2O_3 تكوّن الأكاسيد والانسداد الجزئي للمسام، مؤديًا إلى انخفاض معامل انتقال الحرارة. وتوفر هذه النتائج فهمًا جديدًا لآليات الترسيب التآزرية والتضادية التي تتحكم في تحسين أداء الغليان في الموائع النانوية الأحادية والهجينة.

الكلمات المفتاحية: الموائع النانوية الهجينة، الموائع النانوية، ترسّب الجسيمات النانوية، معامل انتقال الحرارة، الفيض الحراري الحرج.